



HAL
open science

A cavitation-seal mechanism for ultramylonite formation in quartzofeldspathic rocks within the semi-brittle field (Vivero fault, NW Spain)

Marco A. Lopez-Sanchez, Sergio Llana-Fúnez

► To cite this version:

Marco A. Lopez-Sanchez, Sergio Llana-Fúnez. A cavitation-seal mechanism for ultramylonite formation in quartzofeldspathic rocks within the semi-brittle field (Vivero fault, NW Spain). *Tectonophysics*, 2018, 745, pp.132-153. 10.1016/j.tecto.2018.07.026 . insu-03661348

HAL Id: insu-03661348

<https://insu.hal.science/insu-03661348>

Submitted on 5 Mar 2024

HAL is a multi-disciplinary open access archive for the deposit and dissemination of scientific research documents, whether they are published or not. The documents may come from teaching and research institutions in France or abroad, or from public or private research centers.

L'archive ouverte pluridisciplinaire **HAL**, est destinée au dépôt et à la diffusion de documents scientifiques de niveau recherche, publiés ou non, émanant des établissements d'enseignement et de recherche français ou étrangers, des laboratoires publics ou privés.

A cavitation-seal mechanism for ultramylonite formation in quartzofeldspathic rocks within the semi-brittle field (Vivero fault, NW Spain)

Marco A Lopez-Sanchez^{1,2} and Sergio Llana-Fúnez¹

¹Departamento de Geología, Universidad de Oviedo, 33005 c/Jesús Arias de Velasco s/n, Oviedo, Spain

²*Present address:* Géosciences Montpellier, Université de Montpellier & CNRS, CC 60, Place E. Bataillon, 34095 Montpellier cedex 5, France

Corresponding author: Marco A. Lopez-Sanchez

Géosciences Montpellier

Université de Montpellier & CNRS

Campus Triolet cc060

Place Eugène Bataillon

34095 Montpellier Cedex05

France

Tel.: (33) 4 67 14 30 64

Email: marco-antonio.lopez-sanchez@umontpellier.fr

Abstract: Bands of multi-phase mixtures with an extreme grain size reduction called ultramylonites are a common feature in shear zones from the middle crust to upper mantle conditions. Indeed, they are one of the most typical manifestations of strain localization in high-strained polymineralic rocks in the lithosphere, especially in the semi-brittle field. Yet many questions remain on their origin, and existing models either do not explain all the observations or require the introduction of physical processes that are difficult to prove, particularly for the inter-grain mixing of phases. Here we present a case study of ultramylonite bands developed in a coarse-grained granite deformed at conditions near the base of the seismogenic zone, i.e. showing coseismic deformation microstructures overprinted by thermally activated ones. We found that in the mylonite to ultramylonite transition, two deformation mechanisms coexist promoting inter-grain phase mixing through Kfs precipitation: (1) dislocation-accommodated grain boundary sliding in quartz and (2) diffusion-accommodated grain boundary sliding in feldspar. The model proposed to explain grain mixing is based on a cavitation-seal mechanism, which is strongly dependent on grain boundary sliding for the opening of transient micro-cavities and on the diffusivity of potassium feldspar for their progressive sealing.

Keywords: Ultramylonite; grain mixing; disGBS; deformation mechanisms; cavitation; grain boundary sliding

1 Introduction

Deformation in the lithosphere mostly accommodates through planar zones known as shear zones (e.g. Ramsay, 1980; Vauchez et al., 2012). The study of the processes that lead to strain localization in such zones is key to understanding how crustal-scale faults form and evolve over time and, ultimately, how plate tectonics work. One of the most common manifestations of strain localization below the seismogenic zone down to the upper mantle are bands that consist of multi-phase mixtures with an extreme grain size reduction named ultramylonite bands. They are particularly common in quartzofeldspathic rocks within the semi-brittle field (see references in Table 1), although they have also been reported at amphibolite facies (e.g. Behrmann and Mainprice 1987; Fliervoet et al., 1997), or in peridotites deformed at different conditions down to the upper mantle (Hidas et al. 2016; Précigout et al. 2017; Vauchez et al. 2012 and references therein). Despite their importance for understanding strain localization, many questions remain on the origin of the extreme grain size reduction and, especially, the processes that lead to inter-grain phase mixing.

Here we present a case study of ultramylonite bands developed in a coarse-grained granitic host rock deformed in a crustal-scale extensional shear zone in the hinterland of the Variscan Orogeny in NW of Iberian peninsula. Ultramylonites formed in the semi-brittle layer, with tectonites showing coseismic deformation microstructures overprinted by thermally activated ones and vice versa. The significance of this study is threefold:

- At mid-crustal levels, a large portion of the continental crust in many tectonic settings consists of quartzofeldspathic aggregates (granitoids and gneisses). Such lithology is therefore key to understand crustal deformation.

- There is a need to understand and predict how rocks respond to deformation during semi-brittle flow (Reber et al., 2015; Scholz, 1988). Indeed, to date no widely accepted empirical law exists for predicting rock behaviour during semi-brittle flow. Despite recent experimentally based attempts (e.g. Dell'Angelo and Tullis, 1996; Pec et al., 2016), none of them were able to reproduce some of the most common features observed in natural granites. In particular, the syntectonic metamorphic reactions that usually concur with fracturing. In addition, the inherent limitations of deformation experiments in terms of strain rates imply that field-based studies remain essential to validate the empirical laws derived experimentally by comparison of the resulting deformation microstructures. Overall, field-based studies remain key to validate the models of the strength the crust, large earthquake nucleation and propagation, and plate interactions in specific tectonic settings.

- Given the wide occurrence of ultramylonite bands within the lithosphere, there is a need to understand the physical processes and timescales involved during their formation.

The main aim of this study is to propose a model for the formation of ultramylonite bands within the semi-brittle field based on microstructure identification and deformation mechanism interpretation at different stages of deformation.

2 Brief review of ultramylonite band formation

The most obvious features in ultramylonite bands are the extreme grain size reduction and the grain mixing between different mineral phases. Random CPO, although not always observed, is very typical (e.g. Behrmann, 1985; Behrmann and Mainprice, 1987; Boullier and Gueguen, 1975; see also references in Table 1). Any model trying to explain the origin and formation of ultramylonite bands must account for the mechanisms that allow (i) the extreme grain size reduction, (ii) the inter-grain mixing of phases, and (iii) the progressive loss of pre-existing CPO.

The localization and maintenance of deformation in ultramylonite bands requires the band to be weaker than the surrounding material. There is a consensus that the extreme grain size reduction observed in ultramylonites points to a switch from dislocation to grain-size sensitive creep, lowering the strength of the rock and allowing the strain to localize (e.g. Bercovici and Ricard, 2012; Platt, 2015; Rutter and Brodie, 1992; Warren and Hirth, 2006; see also references in Table 1). Yet, the factors controlling how and where ultramylonite bands develop remain poorly understood. In principle, the nucleation of ultramylonites may be triggered by imposed boundary conditions (i.e. inherited “external” factors). For example, near the base of the seismogenic zone, it seems rather typical that ultramylonites nucleate on pre-existing mechanical anisotropies such as brittle precursors (e.g. Mancktelow and Pennacchioni, 2005; Pennacchioni, 2005; Segall and Simpson, 1986; Sullivan et al., 2013; Takagi et al., 2000). Although brittle precursors may account for the origin of some ultramylonite bands, it does neither explain by itself the necessary mechanisms for the generation of the fine-grained matrix and the mixing, nor the origin of ultramylonites in settings where fracturing does not occur. The alternative is that ultramylonite bands nucleate due to intrinsic material response during deformation, i.e. due to reaction-induced weakening or heterogeneous development of a specific rock fabric feature.

The existing mechanisms for grain size reduction are well known: comminution via fracturing (i.e. cataclasis), dynamic recrystallization, and metamorphic reactions. Cataclasis is the dominant mechanism for grain size reduction within the seismogenic zone, although it may be an

important mechanism in some mineral phases outside this zone. Syntectonic metamorphic reactions are often described as a key grain size reduction factor, particularly during semi-brittle flow at mid-crustal conditions (see Table 1), but also in other tectonic settings down to the upper mantle (e.g. Brodie and Rutter, 1987; Rutter and Brodie, 1988; Stünitz and Tullis, 2001; White and Knipe, 1978). Still, not all mineral phases are prone to react in specific environmental conditions and therefore some of them require the support of other mechanisms for reducing the grain size.

Dynamic recrystallization (DRX) is a major process in natural shear zones for grain refinement. It is therefore expected to play a key role during the mylonite to ultramylonite transition. However, the issue whether DRX can promote by itself a switch from a dislocation-dominated to a grain-size sensitive creep, as expected in ultramylonites, remains a long-standing debate. Some authors proposed that such a switch occurs (Behrmann, 1985; Jin et al., 1998; Kirby, 1985; Platt, 2015; Platt and Behr, 2011). In contrast, others agree that this switch might be possible but short-lived because once the grains enter in the grain-size sensitive field will grow to minimize the grain surface-energy (De Bresser et al., 2001; Derby and Ashby, 1987; Pearce and Wheeler, 2011; Shimizu, 1998). So far, large shear (torsion) experiments performed at constant strain rates in monomineralic aggregates within the dislocation creep field produce neither a switch to a grain-size sensitive creep nor strain localization (Barnhoorn et al., 2004; Bystricky et al., 2000; Pieri et al., 2001). In addition, Austin and Evans (2009) found that when diffusion creep dominates in calcite aggregates deformed experimentally the grain growth rates are similar to those of static grain growth. Both observations support the unfeasibility of such switch if grain growth is not inhibited by another mechanism. Another issue with DRX is that the mechanism does not produce by itself grain mixing.

In summary, ultramylonite band formation requires the involvement of any of the available mechanisms to reduce the grain size, either cataclasis, DRX, or metamorphic reaction, and the mixing of grains. If DRX had a significant contribution during mylonitization, it is required the introduction of other mechanisms for grain mixing and likely further grain size reduction. The most cited mechanism for further grain size reduction is inhibition of grain growth due to the presence of secondary particles known as Zener pinning (e.g. Herwegh et al., 2011; Krabbendam et al., 2003; Linckens et al., 2011; Walker et al., 1990). This effect would allow the switch to a grain-size sensitive creep as well as the maintenance of mechanical weakening even in periods of deformation inactivity at moderate/high temperatures (Bercovici and Ricard, 2012). However, an effective pinning of grain growth partly depends on the modal contents of the phases (Sundberg and Cooper, 2008) and requires an efficient inter-grain mixing of phases. Although some authors partially disagree with this model, specifically in the role played by the secondary phases (Platt, 2015), it is

widely supported by observations in both nature and experiments (Barnhoorn et al., 2005; Tasaka et al. 2017).

Regarding the processes that lead to grain mixing in granitoids deformed in the semi-brittle field, few models have been proposed (e.g. Kilian et al., 2011; Platt, 2015; see also Table 1). The most cited mechanisms are dissolution-precipitation processes enhanced by fluids and/or metamorphic reactions coupled with the opening of transient cavities during creep, usually termed in geology as creep cavitation. Yet, the physical processes and timescales required for the mixing process remain poorly understood, and existing models present the following limitations:

i) Most grain mixing models involving creep cavitation do not provide direct evidence of cavitation or disregard how cavities arise during deformation (although see Füsseis et al., 2009; Gilgannon et al., 2017; Kilian et al., 2011; Rogowitz et al., 2016). In turn, most studies suggest grain boundary sliding (GBS) as the main cause for cavitation but rarely provide direct or indirect evidence supporting it, and some GBS models predict phase aggregation instead of mixing during grain switching (Hiraga et al., 2013).

ii) Some mixing models strongly depend on quartz diffusivity (e.g. Kilian et al., 2011; Menegon et al., 2015; Platt, 2015). However, clear and unequivocal evidence on dissolution and precipitation of quartz during ultramylonite formation remains elusive and some natural examples of ultramylonite bands report no quartz precipitation during their formation (Table 1). Moreover, reliable precipitation rate data do not exist for most minerals, neither dissolution rate data for K-feldspar at high-pressures (e.g. U.S. Geological Survey, 2004). In contrast, there are quite a few data on the solubility of quartz in water up to upper mantle conditions (e.g. Manning, 1994). However recent studies have revealed that quartz solubility changes strongly with the addition of common chemical species such as NaCl, KCl, or CO₂ (Akinfiyev and Diamond, 2009; Evans, 2007; Newton and Manning, 2000; Shmulovich et al., 2006). This complex behaviour and the absence of robust solubility models in feldspar makes difficult to predict for now which mineral phases are more prone to diffuse and precipitate at different crustal conditions.

iii) Some authors have proposed that creep cavitation models are unlikely when confining pressure exceeds differential stress (Goetze criterion). Under this condition, deformation would theoretically proceed without the opening of empty spaces or with some processes (creep and/or dissolution and precipitation) counteracting the generation of voids imposed by grain heterogeneities to avoid volume expansion (Edmond and Paterson, 1972; Evans and Kohlstedt, 1995). Differential stress estimates in the crust using quartz and calcite piezometers rarely exceed 250 MPa (e.g. Behr

and Platt, 2014; De Bresser et al., 2002; Kidder et al., 2012; Twiss and Moores, 2007). If these estimates are correct, almost all crustal rocks in the dislocation creep field deform under this condition and deformation models requiring cavitation stay dubious.

Due to the last point, mechanical grain mixing models avoiding the requirement of creep cavitation have been recently proposed (Bercovici and Skemer, 2017). Alternative modes of mixing have also been explored experimentally during deformation at moderate (0.3 GPa) (Tasaka et al. 2017a) and high (1-1.5 GPa) confining pressures (Cross and Skemer, 2017; Linckens et al., 2014). Cross and Skemer (2017) found that mechanical grain mixing without cavitation requires the accumulation of large strains ($\gamma > 17$) to be efficient and to form ultramytonites. Yet, some natural examples of ultramytonite bands accumulating substantially smaller strains show a satisfactory grain mixing, indicating the need for additional phenomena beyond a purely mechanical mixing in some cases. In addition, two experimental studies have documented creep cavitation during deformation at differential stresses below the confining pressures typical of mid-crustal conditions (200-400 MPa) (Dimanov et al. 2007; Rybacki et al., 2008). There are also some examples showing an increase of porosity with strain in natural crystal-plastic shear zones (Fusseis et al., 2009; Géraud et al., 1995; Menegon et al., 2015), questioning the impossibility of opening micro-cavities, at least transiently, during rock deformation under the Goetze condition.

3 Geological setting and sample description

The samples collected belong to a two-mica granite, the Penedo Gordo granite, deformed by a regional crustal-scale extensional shear zone referred to as the Vivero fault (NW of Spain) (Matte, 1968; Parga-Pondal et al., 1967) (Fig. 1). The Vivero fault is an extensional shear zone dipping 60° to the West (the hinterland) developed in the late stages of the Variscan Orogeny and with a minimum dip-slip displacement of 6.55 km at the sample location (Lopez-Sanchez, 2013; Lopez-Sanchez et al., 2015). It puts in contact Ordovician and Silurian metasediments in the hanging-wall with Cambrian metasediments of the Lugo dome in the footwall. Hanging-wall metasediments are in greenschist facies (Bastida et al., 1984; Capdevila, 1969; González-Lodeiro et al., 1981), developing Ky-Chl-Cld-Ms assemblages in high-Al pelites (Lopez-Sanchez, 2013; Martínez et al., 1996; Reche et al., 1998b). Footwall rocks show evidence of high-T low-P metamorphism with andalusite, sillimanite and partial migmatization related to the large intrusion of igneous bodies in the Lugo dome (Capdevila, 1969; Marcos, 2013; Martínez Catalán, 1985).

The Penedo Gordo granite shows a north-south elongated shape, parallel to the Vivero fault (Fig. 1). The granite was emplaced in Early Permian times (c. 291 Ma; zircon U-Pb), syn-tectonically to the Vivero fault (Lopez-Sanchez, 2013; Lopez-Sanchez et al., 2015). The mylonitic foliation is consistent with the orientation and kinematics of the extensional deformation associated with the Vivero fault. The granite formed a metamorphic contact aureole in hanging-wall host rocks, with andalusite and biotite overprinting greenschist facies and staurolite (Lopez-Sanchez 2013; Lopez-Sanchez et al., 2015). The fault displacement, the shear zone thickness, and the minimum period of fault activity limit the average shear strain rate to be within the range 2.68×10^{-13} to 6.50×10^{-15} (Lopez-Sanchez, 2013).

3.1 Specimen features

The Penedo Gordo (PG) granite is a coarse-grained two-mica (mostly biotite) granite (Fig. 2). The granite localizes deformation at outcrop scale in its eastern margin, towards the core of the Vivero Fault, developing ultramylonite bands of up to dm in thickness (Fig. 2). The main constituents of the PG granite are quartz, microcline, plagioclase, biotite and muscovite (Lopez-Sanchez, 2013; Ortega and Gil-Ibarguchi, 1990). The modal fraction of the main phases in the low-deformed samples are (Fig. 2c): ~ 62 % of feldspar (microcline + plagioclase), ~ 35 % quartz and ≤ 3 % micas (mainly biotite). The rock can be primarily described as a two-phase aggregate assuming that the mechanical behaviour of both feldspars is rather similar during deformation (see later) and that quartz and feldspar constitute around 97 % of the rock volume.

Based on a set of identifiable features in hand-specimen, we qualitatively classified the samples into five deformation degrees, outlined below from the lowest to the highest degree of strain (Lopez-Sanchez, 2013; Fig. 2). Grade I samples show no signs of deformation to the naked eye, although there are some on a microscopic scale. Grade II samples show signs of solid-state deformation, such as faint shape fabrics in quartz and intragranular fractures in feldspar. Grade III samples show a widespread fracturing of feldspar and locally flame-like zones enriched in a dark-green microcrystalline phase. Grade IV samples show highly strained areas (dark-grey strongly foliated homogeneous areas) alternating with others in which there is a significant fraction of porphyroclasts. Grade V samples –ultramylonite bands– are formed by a greyish strongly foliated homogeneous matrix when not altered. Grains are indistinguishable in standard thin sections in optical microscopy (transmitted light). Quartz pods show microboudinage.

3.2 Pressure, depth, and temperature constraints

Pressure and temperature during deformation in hanging-wall host rocks were constrained using pseudosections in high-Al graphitic pelites and Al-poor Mn-bearing psammopelites (Lopez-Sanchez, 2013; Martínez et al., 2001). High-Al pelites near the core of the shear zone show a metamorphism evolving from Ky-Cld-Chl-Ms to $St\pm Chl\pm Bt$ assemblages and, locally, to And-Bt $\pm St$ in contact aureoles. The porphyroblast-matrix relations indicate that staurolite, biotite and andalusite grew during the development of the Vivero fault (Lopez-Sanchez, 2013). The potential P - T - t trajectories using thermodynamic modelling reveals that this metamorphic evolution was caused by a nearly isobaric heating event (e.g. fig. 4e in Martínez et al., 2001). This means that hanging-wall rocks did not vary significantly their burial depths during the fault movement at this stage, and that most fault displacement was accommodated by the uplift and denudation of the footwall rocks, in agreement with the pure decompressional P - T - t path found in the footwall rocks within the Lugo Dome (Reche et al., 1998a).

The development of a contact aureole with andalusite and biotite in hanging-wall rocks indicates that the pressure during the granite deformation remained below the Al_2SiO_5 triple point, located somewhere between 380 MPa (Holdaway, 1971; Holdaway and Mukhopadhyay, 1993) and 450 MPa (Pattison, 1992). The crystallization of staurolite prior to andalusite and biotite impose a P - T - t path that implies a minimum pressure during the hanging-wall deformation of about 300 MPa (Martínez et al., 2001). In summary, considering metamorphic pressure as lithostatic (i.e. mean stress (P) \approx vertical stress) the pseudosection analysis limits the pressure during the Penedo Gordo deformation to be between 300 and 450 MPa, indicating depths between 11.3 and 15.5 km (g of 9.8 ms^{-2} and an average rock density of 2700 kg m^{-3}).

Regarding the minimum temperature during deformation, the St - in line calculated for host rocks provides a minimum T during deformation of about $400 \text{ }^\circ\text{C}$ (Lopez-Sanchez, 2013). However, as recorded in the contact aureoles, the temperature in host rocks was locally higher in space and time due to the concomitant magmatism during the Vivero fault activity (Lopez-Sanchez et al., 2015).

4 Methods

4.1 In situ geochemical analysis and phase maps

In-situ geochemical analyses and compositional mapping were carried out on a five-spectrometer Cameca SX100 electron microprobe (EPMA) at the University of Oviedo. Maps and

in-situ analysis involved count times in the range 0.1 to 0.5 s and a current of 100 nA. Maps range from 256x256 to 512x512 μm^2 , with a step size of 1 μm .

4.2 Image acquisition and analysis

Images for microstructural analysis were obtained from different sources: (i) a Leica DC500 digital camera attached to a polarized light microscope, (ii) a scanning electron microscope (SEM) model JEOL-6610LV in BSE mode (20kV, spot size 40), and (iii) a Cameca SX100 electron microprobe, all of them at the University of Oviedo.

Image enhancement and measurements were carried out using the public domain software ImageJ2 (Rueden et al., 2017). Data analysis from the ImageJ2 output were made using Numpy and Scipy Python scientific libraries (Oliphant, 2007) and the GrainSizeTools script v.1.3.4 (Lopez-Sanchez, 2017). The methods used to estimate grain size and the shape of the grain size distribution via the multiplicative standard deviation (MSD) value are detailed elsewhere (Lopez-Sanchez and Llana-Fúnez, 2016, 2015). Briefly, the MSD value measures the asymmetry of the grain size distribution. An MSD value equal to one corresponds to a normal distribution, and values above one with lognormal distributions, being the higher the value the greater the asymmetry. The modal content of the different mineral phases in the ultramylonites was estimated combining different elemental EPMA maps (K, Na, Fe, or Ca) to generate phase maps in false-colour images. The areas were later measured using the ImageJ2 software.

Two shape descriptors were used for grain shape analysis. The aspect ratio, measured as the ratio between the maximum and the minimum feret (calliper) diameters. The feret diameters are defined as the largest and the shortest distance between any two parallel tangents on the particle, respectively. The solidity, defined as the area of the grain profile divided by the convex hull area of the grain profile, which measures the overall concavity of the particle and thus the morphological irregularity of the grain. Box plots (Tukey, 1977) and histograms were used for comparative purposes between the different phases. The boxes indicate the interquartile range (IQR), the whiskers the data within the 1.5 times the IQR range, and the empty dots the values outside that range.

Particle spatial analysis was performed in quartz using the nearest-neighbour analysis to discriminate between random, clustered and regular (or anti-clustered) distribution of grains in the ultramylonites. Specifically, we used the mean Euclidean distance between closest pairs of centroids (Schwarz and Exner, 1983). To estimate the degree of randomness, clustering or regularity of the distribution of grains in space, we use the index value (D), estimated dividing the actual mean nearest-neighbour distance (d) by the expected mean in a random distribution (d_e) ($D=d/d_e$) (e.g.

Clark and Evans, 1954; Davis, 2002; Jerram et al., 1996; Kretz, 1969). Thus, a D value equal to one corresponds to particles distributed randomly. D values smaller than one correspond to particles with some degree of clustering (from 0 to 1), and D values larger than one (up to a maximum value of 2.149) to particles with certain degree of dependence or regularity. We provide plots comparing the actual distribution of the actual nearest neighbour distances to a perfect random (Poisson) distribution, and a density 2D map showing the distribution of centroids. For more details in the nearest neighbour, analysis (including Python source codes) see supplementary material.

4.3 Analysis of crystallographic-preferred orientation

4.3.1 Sample preparation

Ultramylonite sample MAL07 thin section was cut oriented with the lineation parallel to the long axis of the glass and perpendicular to the foliation (XZ section). Note, however, that the foliation in thin section MAL07 shows an angle (62°) respect to the long axis of the thin section glass. The rock slab was polished down to 30 μm thick and then re-polished first with diamond powder and then with colloidal silica to remove surface damage (Lloyd, 1987). Thin section was carbon coated (~ 2 nm) and the edges of the section painted with conductive carbon paint to prevent charging. We consider the selected areas for analysis to be representative of the overall microstructure in thin section.

4.3.2 EBSD analytical conditions

Full crystallographic preferred orientation (CPO) was measured by indexing Electron Backscattered Diffraction (EBSD) patterns in an electron microscope fitted with a field emission gun at the SEM-EBSD facility of Centro de Instrumentación Científica at the University of Granada. EBSD patterns were collected using a 20 kV acceleration voltage, a beam current of 30 nA, and a working distance of 12-15 mm. Data were acquired using the Aztec software package CHANNEL (HKL technologies, Oxford Instruments). High-resolution orientation maps were obtained using step sizes between 0.5 and 2 μm , ensuring that grains contained ample measurement points. Only quartz was indexed since the quality of the Kikuchi patterns for feldspars was insufficient for a reliable indexing. Non-indexed points essentially correspond to grain boundaries, cracks and other mineral phases such as feldspar and biotite.

Post-acquisition data treatment was performed using the MTEX toolbox v4.5 in Matlab (Bachmann et al., 2010; Mainprice et al., 2014). For details in the workflow, see Supplementary material. CPO data is plotted in equal-area upper hemisphere pole figures based on the mean orientation of each grain to avoid over-representation of large crystals. Pole figures were contoured

as multiples of a uniform density. CPO texture strength and randomness was estimated using two indexes, one based on the orientation distribution function, the J index (e.g. Mainprice et al., 2014), and another based on the misorientation analysis, the M-Index of Skemer et al. (2005). Bandwidth and half-widths for the J index were estimated using the de la Vallée Pousson kernel (Bachmann et al., 2010).

5 Microstructure from low to high strain domains

For simplicity, the microstructures of the main phases are described separately, classifying the amount of strain into three groups: i) low-strain samples (Grades I and II), mylonites (grades III and IV) and ultramylonite bands (grade V). The term mylonite refers here to a strongly deformed rock with a planar foliation formed predominantly by crystal-plastic flow but with some minerals suspended in the matrix deforming by brittle fracturing (e.g. Passchier and Trouw, 2005).

5.1 Low-strain samples

5.1.1 Quartz

Quartz grain size is larger than a centimetre. The occurrence of blocky sub-grains (chessboard extinction) is common (Fig. 3a). Grain boundaries are irregular with clear examples of bulging (Fig. 3b, c), typical of a strain-induced grain boundary migration mechanism. Some small strain-free grains appear along the quartz-quartz grain boundaries (Fig. 3c). Fluid inclusions are abundant and, in some cases, they are aligned (Fig. 3b, c).

5.1.2 K-feldspar (Or_{95-97})

K-feldspar (Kfs) develops solid-state deformation microstructures such as flame perthite, tartan twinning, and intragranular fractures, being flame perthite the dominant deformation microstructure. In grade I samples, flame perthites nucleate first at grain boundaries and fracture surfaces (Fig. 3d). With the increasing of strain (grade II), flame perthites affect the entire grain, first following one crystallographic plane and then becoming widespread and following, in some cases, two crystallographic planes (Fig 3e, f). Tartan twinning develops at grain boundaries and, although common, rarely affects the whole crystal. The presence of intragranular fractures is rather limited, occasionally showing very fine albite and, less often, biotite grains along them (Fig. 3d, e).

5.1.3 Plagioclase (An_{16-23})

The most common features are undulose extinction and sub-grain walls (Fig. 3h). They also display a limited number of intragranular fractures. Myrmekites are poorly developed (Fig. 3i). Feldspar-feldspar boundaries sometimes appear very irregular, developing bulging or even new very-fine feldspar grains (Fig. 3g).

5.2 Mylonites

5.2.1 Quartz

Quartz grains develop shape fabric and show polygonization due to dynamic recrystallization (DRX) processes (Fig. 4). Undulose extinction and sub-grains are well developed. New grains initially originate at grain boundaries and inside the grains in the form of strings (Fig. 4a-c). The quartz strings are extensions of fractures in the adjacent feldspars (Fig. 4a), in a similar fashion to those produced experimentally in Trepmann et al. (2007). In some places, blocky sub-grains are still visible displaying elongated shapes due to deformation (Fig. 4c), indicating that their development precede the DRX in quartz. Recrystallized grains show polygonal equant shapes (i.e. foam-like microstructure) mostly free of internal deformation (Fig. 4f, h). Grain orientation spread (GOS) per grain (Wright et al., 2011) is $\geq 99\%$ below 1.7° , indicating a low intracrystalline lattice distortion typical of recrystallized grains (Cross et al., 2017a). Some grains reach GOS values up to 5.7° , but these mainly correspond to grains not reconstructed properly due to touching grains with low misorientations ($< 10^\circ$) or to relic grains. In samples with deformation of grade IV, the recrystallization of quartz appears complete (Fig. 4d-f).

The recrystallized grain size and its distribution were studied elsewhere (Lopez-Sanchez and Llana-Fúnez, 2016, 2015). A summary along with information on shape parameters is provided in Table 2 and Figure 5. Briefly, the mean apparent grain size is $35.8\ \mu\text{m}$ and the lognormal shape of the distribution yields an MSD value of 1.65 ± 0.05 (Fig. 5c). Grain fractions below $20\ \mu\text{m}$, as measured in the ultramylonite matrix (see section 5.3), represent the 2.01% of the total quartz volume in the mylonites (Fig. 5b).

Recrystallized grains show CPO (Fig. 6). Quartz [c]-axes arrange to form a single great girdle with a maximum close to the Y-axis and a tendency to spread along the Y-Z plane, although the girdle is somewhat asymmetric. Quartz <a>-axes maxima appear at the margins. However, the expected three clear maxima cannot be recognized, suggesting that no preferred “single crystal” orientation exists for the crystals oriented with the [c]-axes parallel or close to the Y direction. Overall, this indicates the main operation of prism, and to a lesser extent, rhomb and basal <a> slip. The CPO strength based on several indexes indicates a moderate CPO strength (Table 3).

5.2.2 *K-feldspar (Or₉₅₋₉₇)*

Kfs fracturing becomes widespread, following two dominant planes (Fig. 7, see also 4a, b). Fractures accommodate displacement and are transgranular. Patchy undulose extinction and sub-grain boundaries occur. Small albite grains and, to a lesser extent, biotite crystallized along fractures and grain boundaries (Fig. 7a-f), increasing their modal fraction with strain. Backscatter electron microscope images reveal that albite-oligoclase patches locally replace the original K-feldspar (Fig. 7d).

5.2.3 *Plagioclase (An₁₆₋₂₃)*

As in Kfs, fracturing becomes widespread and follows two main planes but, in this case, one becomes predominant (Fig. 7g). Fractures accommodate displacement across several grains. Inside the grains, patchy undulose extinction and sub-grain limits occur. In contrast to Kfs, small Kfs and biotite grains crystallized along fractures and at grain boundaries. In this case, the presence of biotite along fractures is more noticeable than in Kfs fractures (Fig. 7g, h). New Kfs grains sometimes show very irregular or film-like shapes when filling dilatant sites (Fig. 7i, j). Fractures in plagioclase differ from those in Kfs as they commonly show a network of small-scale fractures that generate a notable porosity within the grains (Fig. 7h, i). Some plagioclase grains show sericitic alteration (Fig. 7g, h), but this reaction product is absent in the matrix or along fractures.

5.2.4 *Dark veins*

Some mylonitic samples show irregular dark veins enriched in very fine-grained dark-green biotite and breccia cutting across the mylonitic foliation with neat or, less frequently, irregular margins (Figs. 2e and 7k). Margins usually appear darker in hand specimen and in thin section. The clasts within the veins show no size or shape sorting, ranging from rounded to highly angular.

5.2.5 *Temperature estimates during mylonitization*

Temperatures during mylonitization were estimated using the composition of feldspars in the fractures and the ternary-feldspar thermobarometer (Green and Usdansky, 1986) (Fig. 7k). The thermobarometer yields temperatures within the range 425-475 °C, in agreement with the estimates obtained from the hanging-wall host rocks (roughly within 400-500 °C) and the deformation microstructures. This also indicates that the Penedo Gordo granite and the hanging-wall host rocks reached a thermal equilibrium before mylonitization.

5.3 **Ultramylonite bands**

The matrix in ultramylonites consists mainly of a mixture of very fine grains of K-feldspar (34%), albite (30%), quartz (25-30%), biotite (2-8%), and epidote (<1%) (see supplementary material). Quartz pods made up of recrystallized grains are common (Fig. 8a). Small isolated feldspar porphyroclasts rarely appear. During the transition from low-strain granite to ultramylonitic bands, the modal fraction of feldspar remains nearly constant. In contrast, there is a slight increase in biotite content, varying locally from $\leq 3\%$ up to 8%, and a slight decrease of quartz content. Despite the mica increase, biotite grains always appear as strongly oriented isolated mica flakes in the matrix (e.g. Fig. 8).

BSE images reveal that quartz aggregates gradually disintegrate into the surrounding polycrystalline matrix. Inside the aggregates, Kfs appear at triple junctions (Fig. 8c), grain boundary jogs, and between quartz grain boundaries, sometimes displaying very irregular or film-like shapes (Fig. 8c, d, e). In contrast, we found no evidence of voids caused by dislocation pile-ups (Zener-Stroh cracking) in our thin sections (e.g. Gilgannon et al., 2017; Rogowitz et al., 2016). Kfs isolates quartz grains nearby the aggregates by surrounding them. In such cases, quartz grains display smaller apparent grain sizes (Fig. 7b, d). BSE-SEM images show the progressive isolation of quartz grains away from the aggregate margins (Fig. 8e).

Image analysis show that quartz grains remain as near-equant with well-ended crystal faces during the mylonite to ultramylonite transition (Figs. 5e, f). In contrast, quartz grains reduce significantly in size (Fig. 5a), change the shape of the grain size distribution being less asymmetrical in the ultramylonites (cf. Figs 5c and d), and loose completely the CPO (Fig. 6, Table 3). In addition, the nearest-neighbour analysis indicates that the spatial distribution of quartz grains within the well-mixed polymineralic matrix is random (Fig. 10); with index D values of 1.05 ± 0.04 (2σ level) using a Poisson model, and 1.02 ± 0.06 (2σ level) using a Monte Carlo simulation (see Supplementary material for details).

Regarding feldspars, Kfs and albite in the polymineralic matrix have apparent grain size distributions that partially overlap, but with Kfs showing a wider range towards larger sizes (Fig. 9a). The range of AR values is very different from quartz, yielding higher median values (i.e. more elongated) and further variability (i.e. wider interquartile ranges) (Fig. 9d). This is very distinctive in the case of Kfs, which shows a long tail towards high AR values. Frequent values above 3.0 or even 4.0 are related to the presence of film-like grains. The long axes of feldspar grains show a clear preferred orientation and align with the tectonic foliation defined by the biotite flakes. Regarding the irregularity of grain boundaries, both feldspars show similar solidity median values typical of grains with regular morphologies. However, there is a notable difference in the range of values between Kfs

and albite, since Kfs take values down to 0.5. These low solidity values reflect the fact that locally some Kfs grains show very irregular shapes. In fact, most Kfs grains represented in figure 9c were measured in Kfs-rich bands where very irregular Kfs grains are less common, making low solidity values in Kfs under-represented (see grain boundary maps in the supplementary material).

6 Discussion

6.1 Interpretation of microstructural evolution: from proto- to ultramylonite

The deformation history of the Penedo Gordo granite can be separated into two main stages: an early *HT* stage and an overprint at moderate *T* partially in semi-brittle conditions. In turn, the second stage includes three well-differentiated stages: i) a widespread semi-brittle deformation, ii) a mylonitization stage, and iii) an ultramylonitization stage, the last two involving strain localization.

6.1.1 High-temperature deformation stage

The granite displays few *HT* deformation microstructures that are incompatible with the overprinting fracturing in feldspar or with the type of dynamic recrystallization that is observed in quartz. These *HT* microstructures include blocky sub-grains in quartz, typical of granite sub-solidus deformation (Kruhl, 2003), and some evidence of grain boundary mobility in feldspars due to DRX (see Fig. 3g). These microstructures very likely developed during the granite emplacement and prior to granite cooling.

6.1.2 General semi-brittle deformation stage

The semi-brittle deformation stage induces phase transformations and fracturing in feldspar. Fractures remain essentially intracrystalline and do not produce comminution. Stresses induce chemical changes in both feldspars, most notably flame-shaped perthites in Kfs grains. The presence of a patchy undulose extinction and sub-grains in both feldspars prevents us to infer directly whether dislocation creep played a role in feldspar deformation since similar microstructures due to microfracturing and healing of arrays of microcracks were reported elsewhere (den Brok et al., 1998; Tullis and Yund, 1987). Dislocation creep and DRX accommodate deformation in quartz. DRX induces local grain boundary migration in quartz, yielding irregular grain boundaries, bulging, and some very fine grains along quartz-quartz grain boundaries. In any event, DRX is limited.

At this stage, feldspars are the main (vol. 62 %) and strongest phase, and deformation in quartz was limited to very small volumes nearby grain boundaries. Feldspars mainly supported the strength of the granite; i.e. a framework supported rheology in the sense of Handy (1990, 1994).

High stress microstructures in feldspar, such as flame perthites and fractures, supports this interpretation.

6.1.3 Mylonitization stage

During this stage, feldspars display multiple evidence of fracturing coexisting with the crystallization of new phases (neocrystallization) along fracture surfaces. Some microstructures can be regarded as coseismic in origin, placing the development of the mylonites close to the base of the seismogenic zone. For example, the geometry and contacts of biotite-rich dark veins with breccia shown in figures 2e and 7k resemble pseudotachylytes. Despite the absence of typical features of pristine pseudotachylytes (glass, sulphide/oxide droplets, spherulites, etc.), some typical features of recrystallized ones can be identified. These include quenched margins, embayed edges at the margins, clasts with no size or shape sorting, and bulk chemistry enriched in hydrous minerals -e.g. biotite- relative to the host rock (Kirkpatrick and Rowe, 2013; Price et al., 2012). Further, several authors (Jiang et al., 2015; Maddock, 1992; Moecher and Sharp, 2004) reported similar biotite enrichment in pristine undeformed pseudotachylytes.

Dynamic recrystallization dominates in quartz. The strings of recrystallized quartz grains aligned with clear fractures in feldspar grains (Fig. 4) resembling those experimentally produced by Trepmann et al. (2007) and Trepmann and Stöckhert (2013). This observation along with the presence of pseudotachylyte indicate that coseismic microstructures coexisted with the recrystallization of quartz (Fig. 4a-c), and that at some point during the mylonitization stage the granite suffered a combination of brittle deformation due to quasi-instantaneous loading with periods of slow creep in between (e.g. Jiang and Lapusta, 2016; Scholz, 2002).

A striking observation in mylonites is that new albite appears only at Kfs fracture surfaces while new Kfs crystallized between plagioclase and quartz (Fig 7c). To explain this, we suggest different mechanisms of formation for both feldspars. The irregular shapes of Kfs and the presence of biotite indicate that the precipitation of these mineral phases sealed the porosity generated during feldspar fracturing. Consequently, the mechanism of formation of fine-grained Kfs was metamorphic reactions and thus the balance between the rates of nucleation and the grain growth controlled their grain size. The fine grain size of Kfs suggests a high nucleation rate. The small change in K-feldspar composition, the places where the new Kfs grains appears preferentially, and the presence of new mineral phases (e.g. biotite \pm epidote) discard DRX as a grain size reduction process.

Figures 7d-f suggest a different mechanism for the generation of fine-grained albite. Kfs albitizations nearby fractures (Fig. 7d) indicate compositional changes during deformation typical of

an interface-coupled dissolution-precipitation mechanism (e.g. Hövelmann et al., 2009; Putnis and John, 2010). The fracturing in Kfs clearly favoured this mechanism, increasing the surfaces available and the permeability of the rock for the progress of the mineral reactions. We suggest the following reaction, very similar to that proposed by Ree et al. (2005), for the interface-coupled dissolution-precipitation mechanism. A Na-rich fluid enters the rock during feldspar fracturing allowing Kfs to be replaced by albite nearby fracture surfaces. The mineral reaction can be represented using ideal formulae by:



This reaction releases K^+ into the fluid, increasing its content or keeping the fluid saturated in potassium during deformation. Figure 7d indicated that in some cases the albitization predates the comminution resulting in the formation of fine-grained albite. In contrast, the microstructures in figures 7e and f admit two interpretations: (i) albite crystallized directly at feldspar fractures or (ii) comminution and then the albitization of fine-grained Kfs generates the fine-grained albite. We suggest that the last interpretation is more likely since it agrees better with the angular aspect of some grains, which indicates comminution, the mixture of Kfs and albite grains shown in figure 7f, and the Kfs albitization in figure 7d. Overall, this suggests that the mechanism that controlled the starting grain size of fine-grained albite was comminution.

Dislocation creep accommodated deformation in quartz and the dominant mechanism of grain size reduction indicates sub-grain rotation recrystallization. An estimate of differential stress based on the grain size piezometer of Stipp and Tullis (2003) yields 36.3 MPa, a value well below the expected value for an area near the brittle-plastic transition in the continental crust (e.g. Behr and Platt, 2014; Brudy et al., 1997; Gleason and Tullis, 1995; Kidder et al., 2012; Kohlstedt et al., 1995). This value along with the foam-like microstructure suggest that these samples underwent some degree of annealing after mylonitization.

Regarding the macroscopic behaviour of the granite, three rheological domains contribute and compete at this stage: (i) the feldspar framework, (ii) the recrystallized quartz aggregates, and (iii) the fine-grained polymineralic matrix. The feldspar framework deforms in a brittle manner and is the strongest domain. Its contribution to the bulk strength of the rock decreases gradually during this stage due to fracturing and chemical reactions. The quartz domain behaves as a power-law creep material and therefore has a lower strength than that of the feldspar framework. According to Bons and Urai (1994), the connection of a single phase in a deformed aggregate requires a minimum 25 % of volume after 50 % of shortening. This means that the contribution of the quartz domain (~35%) to

the bulk strength of the rock was dominant at some point, as evidenced by the formation of a compositional layering. The change in the rheology is potentially fast since it depends on reaching a grade of finite strain necessary to connect the weak matrix (Handy, 1990, 1994). The fine-grained well-mixed polymineralic matrix deformed by a grain-size sensitive creep (see section 6.2). Hence, it represents the weakest of the three domains. Its influence on the bulk strength of the granite was rather limited at this stage due to its small volumetric contribution. Overall, at this stage the granite evolved from a feldspar framework supported rheology to a matrix-supported material mainly controlled by dislocation creep in quartz.

6.1.4 *Ultramytonitization stage*

Ultramytonite bands represent the final stage of strain localization. The outcrop in Figure 2a displays ultramytonite bands arranged in patterns that may suggest brittle precursors controlling the ultramytonite band nucleation, but this hypothesis requires further study. Biotite content increases from 3 up to 8% in ultramytonites, but given that biotite grains appear always as isolated mica flakes it is unlikely that this increase contributes in any significant way to mechanical weakening. However, it is indicative of an increase in the water content in the system. There is also a decrease of 5-10 % in the content of quartz respect to the original photolith.

The increasing of strain during mylonitization led to compositional layering due to the connection of pre-existing volumes enriched in similar mineral phases (Fig 8a). Hence, key issues to explain during the mylonite to ultramytonite transition include:

- i) How monomineralic bands disaggregate and incorporate into the fine-grained well-mixed polymineralic matrix?
- ii) How quartz grains decrease their size anew to reach a very fine grain size with a very distinctive grain size distribution?

We advance that the fine-grained phase mixtures deformed by a combination of fluid-assisted diffusion-accommodated (feldspars) and dislocation-accommodated (quartz) grain boundary sliding. However, the progressive isolation of quartz grains into the matrix (Fig. 10) and its smaller volumetric contribution compared to feldspars suggest that overall the fluid-assisted diffusion-accommodated GBS ultimately controlled bulk rheology and thus the strength of the ultramytonite bands.

6.2 The development of ultramytonite bands

6.2.1 *The disaggregation of quartz aggregates and deformation mechanism in quartz*

Quartz aggregates show the following significant features: (i) a weak CPO; (ii) near-equant polygonal shapes; (iii) essentially monomineralic but with secondary phases at triple junctions and grain boundary jogs; and (iv) notably smaller grain sizes at pod margins and quartz grains nearby.

The boudinage of quartz pods indicates that polycrystalline quartz had different rheology than the surrounding fine-grained polymineralic matrix. This observation points to two potential deformation mechanisms for quartz pod development: dislocation creep and grain boundary sliding. The higher strength of quartz aggregates with respect to the polymineralic matrix and the CPO, despite being weak, suggests that dislocation creep played some role during deformation. The presence of Kfs and Bt at triple junctions requires either the creation of transient micro-cavities with the coupled precipitation of secondary phases (e.g. Kilian et al. 2011) or the solid-state migration of surrounding minerals along quartz grain boundaries (e.g. Bercovici and Skemer, 2017). The following observations however do not support the solid-state model proposed by Bercovici and Skemer (2017) for this case:

- i) The existence of only one feldspar type (Kfs) between quartz grains despite existing areas where albite and quartz-rich bands are adjacent. According to the solid-state model, both feldspars should be observed.
- ii) The solid-state model does not predict by itself the weakening of CPO observed in the quartz pods. In contrast, the operation of grain boundary sliding would explain both the necessary mechanism for opening transient cavities at triple points, grain boundaries jogs, and asperities (e.g. Bourcier et al., 2013; Ree, 1994) and the weakening of CPO due to “external” grain rotations.
- iii) During the mylonitization stage, there is ample evidence of Kfs sealing fractures as soon as they formed, indicating that diffusion of potassium through a fluid and Kfs precipitation were both efficient processes for inter-grain phase mixing at the strain rates at which the Vivero shear zone developed.

The irregular shapes and the necking structures in the interstitial Kfs (cf. Fig. 8c, d vs. Fig. 11c, d) agree with the assumption of a continuous generation of transient creep cavities due to GBS and the coupled sealing with Kfs (Fig. 11). Yet, GBS needs a mechanism to accommodate the rotation of the grains, either dislocation (Rachinger or dislocation-accommodated GBS) or diffusion creep (fluid-assisted or solid-state-Lifshitz GBS) (Fig. 11). Several pieces of evidence support dislocation over diffusion as creep mechanism. As noted above, the higher strength of the quartz pods respect to the surrounding matrix (i.e. the boudinage) and the preservation of a certain degree

CPO suggest dislocation creep. The lack of shape fabrics in quartz also supports dislocation-accommodated grain boundary sliding (disGBS) (Langdon, 2006). Lastly, the absence of evidence of synkinematic quartz precipitation also agrees with this interpretation. Overall, this means a switch from dislocation creep to disGBS occurs in quartz in the mylonite to ultramylonite transition and that this switch is the result of the reduction in grain size imposed by DRX. The disGBS mechanism has been identified experimentally in rocks (Hansen et al., 2011; Hirth and Kohlstedt, 1995; Rutter et al., 1994; Schmid et al., 1977; Tasaka et al. 2017a) and similar transitions have been previously inferred to have occurred in nature (Behrmann and Mainprice, 1987; Miranda et al., 2016; Warren and Hirth, 2006).

The change in the deformation mechanism and the precipitation of secondary phases may result in a further decrease in average grain size due to pinning. However, it seems difficult to justify the marked change in size between the quartz in the pods and grains nearby (Fig. 7a, b, and d). The later annealing event suggested by the small value of differential stress and the foam-like microstructure may explain this abrupt difference in size. This would result from selective crystal growth in the monomineralic quartz domains, while the growth of isolated grains would be inhibited due to the pinning effect. This condition prevents us from knowing the actual difference in the average size between the original recrystallized grains, the grains in the pods, and the dispersed ones. Still, the progressive loss in the strength of the CPO in quartz during the mylonite to ultramylonite transition indicates a change in the deformation mechanism and thus points to a likely change in the average grain size.

Regarding dispersed quartz, the operation of disGBS in the pods at the very same conditions makes disGBS a likely candidate as well. An alternative option would be the mechanism proposed by Kilian et al. (2011), where new quartz grains formed and mixed through a dissolution and precipitation mechanism. The absence of evidence of synkinematic quartz precipitation at any stage during deformation and the near-equant grain shapes (e.g. Langdon, 2006) support the disGBS mechanism over the dissolution-precipitation one. The polygonal shapes also exclude quartz precipitation but this could be the result of a late annealing process. The complete loss of the pre-existing CPO in the dispersed grains is compatible with a disGBS mechanism as well, suggesting that isolated quartz grains reached a critical grain size in which large “external” grain rotations dominate over lattice rotations imposed by dislocation creep. Cross et al. (2017b) have observed a similar behaviour in experimentally deformed quartz-albite mixtures.

Based on the reasoning above, a further grain size reduction in quartz required the coupled operation of disGBS and the cavitation-seal mechanism for pinning grain boundary mobility.

Although no direct evidence exists on quartz dissolution at any stage of deformation, the decrease in the quartz content measured in the ultramylonites indirectly suggests that dissolution may have played some role in reducing grain size. Yet, the near-equant grain shapes suggest that the dissolution of quartz was not crucial for the grain size decrease, but this requires further study on quartz grain surfaces for confirmation. In addition, the disaggregation of quartz pods can be explained solely based on the continuous generation of transient creep cavities due to GBS and on potassium feldspar precipitation for progressively sealing them as soon as they open without requiring quartz precipitation (Fig. 11).

6.2.2 *Deformation mechanisms and disaggregation of feldspar-rich bands*

The mechanism to deform and disaggregate the albite and Kfs-rich bands into the polymineralic matrix (e.g. Fig. 8a, 10a) must be essentially different from that proposed for quartz aggregates. The precipitation of irregular and film-like Kfs between albite grains also indicates creep cavitation and thus the operation of GBS during deformation. However, the elongated appearance of albite grains excludes large rotations during GBS and point to diffusion-accommodated GBS instead (Langdon, 2006), either fluid-assisted or solid-state (cobble creep). Interestingly, albite grains in the albite-rich bands systematically display pitted grain boundaries on polished surfaces, a phenomenon related to transfer by diffusion or the presence of a thin fluid film along grain boundaries (e.g. Gifkins, 1978; Viegas et al., 2016). These features suggest diffusion creep accommodating GBS in albite-rich bands. However, the lack of high-resolution EBSD or TEM data in albite prevents us from definitively ruling out a disGBS mechanism. Lastly, since there is no evidence of albite precipitating within quartz- or Kfs-rich bands at any deformation stage, the diffusivity of albite seems to be limited to local scales (i.e. the surrounding grains).

The mechanism we propose for the destruction of albite-rich bands requires the opening of transient pull-apart micro-cavities between grains as touching grains separate due to grain sliding and their progressive sealing with Kfs (Fig. 12). This separation can also be inferred from the destruction of crystal monolayers (layers of one grain's width) in two-phase rock mixtures deformed experimentally at large strains (Cross and Skemer, 2017). We also observe disrupted albite monolayers in our thin sections (e.g. Fig. 8a), supporting this mechanism. The opening and sealing of pull-apart micro-cavities require the coupling of GBS with Kfs precipitation. However, GBS in feldspars cannot lead to notable grain rotations as for quartz, since the albite-elongated shapes will block them, but just accommodate the “geometrical” necking process imposed by the strain field (Fig 12). In accord, numerical tests predict that diffusion creep either produced in solid-state or assisted by fluids do not inherently produce large grain rotation during deformation (Wheeler, 2009) and

there is experimental evidence of no rotation during diffusion-accommodated GBS in metals (see figure 5 in Langdon, 2006). The opening of pull-apart cavities can also promote the progressive displacement of adjacent grains of other phases in solid-state to dilatational sites, acting as a secondary (i.e. much less efficient) mechanism for mixing (Fig. 12).

Regarding K-feldspar, it is difficult to infer if GBS played a major role during deformation since the main evidence of GBS in quartz and albite was the interstitial precipitation of Kfs due to creep cavitation. Despite this, it seems reasonable to assume that the dominant deformation mechanism was the same one that operated in albite. The operation of GBS coupled with Kfs precipitation would explain the elongated shapes in Kfs (Fig. 12), and this is compatible with the general precipitation of Kfs observed during the different stages of deformation. Alternatively, a solid-state (Coble creep) diffusion-accommodated GBS deformation mechanism would also be compatible.

6.2.3. The inter-grain mixing model

We propose a mixing model that relies on transient cavitation due to the mechanical separation of grains during deformation, and on potassium feldspar diffusivity for progressively sealing the cavities. The mode of deformation was different for feldspar and quartz aggregates during mylonite to ultramylonite transition, coexisting two mechanisms: dislocation-accommodated GBS in quartz and diffusion-accommodated GBS in feldspars. The evidence of Kfs precipitation sealing the porosity during the mylonitization stage is solid, and this supports the same process for the ultramylonitization stage since similar conditions (stress, fluid composition, T , and P) are expected. Theoretically, if Kfs dissolution/precipitation rates are efficient, the deformation can proceed without volume expansion meeting the Goetze criterion. Indeed, the confining pressure in the study case (between 300-450 MPa) likely exceeded the imposed differential stress during creep stages.

The cavitation-seal mechanism predicts the mixing of quartz and albite with Kfs despite their different deformation mechanisms and that Kfs will develop elongated grains compare to albite, both observed features in the ultramylonite samples (Figs. 9d, 12). It also anticipates that the disaggregation of Kfs-rich bands requires much larger strains than in the case of albite- or quartz-rich layers since only a pure mechanical mixing mechanism (i.e. solid-state) applies. Indeed, examples of persistent Kfs-rich bands without the presence of quartz or albite grains exist in our ultramylonite thin sections (Fig. 13), and this feature has been observed in other quartzofeldspathic ultramylonites too (e.g. Ishii et al. 2007 or fig. 9a in Kilian et al., 2011). The persistence of the Kfs-rich bands also suggests that neither quartz nor albite precipitation was determining factors for grain mixing in this

example. Yet, the persistence of specific mineral bands will ultimately depend on which of the different mineral phases involved during deformation have the fastest rate of precipitation and thus on environmental conditions such as T , P , or fluid composition.

This inter-grain mixing model shares similarities with the mixing model proposed by Kilian et al. (2011), but it essentially differs from the mechanism that leads to the mixing of quartz and feldspar into the fine-grained matrix. Kilian et al. (2011) proposed that quartz dissolution and precipitation are necessary for mixing and reducing the grain size of quartz despite they find no direct evidence of quartz precipitation or dissolution. This also requires the input of a new deformation mechanism in quartz. In contrast, our mixing model only requires the operation of a disGBS mechanism coupled with the interstitial precipitation of Kfs (\pm Bt) for the breakdown of quartz aggregates. The slight decrease in quartz content observed in our ultramylonites suggests that quartz dissolution may have played some secondary role for further grain size decrease, as in Kilian's model, but quartz precipitation is not essential for the mixing. In addition, our model provides a satisfactory explanation for two observable phenomena: why quartz grains develop equant shapes and feldspars elongated, and why the persistence of Kfs-rich band over the quartz and albite-rich bands.

7 Conclusions

We propose a model for compositional layer destruction and inter-grain phase mixing during the ultramylonite formation that involves:

- 1) The continuous opening of transient micro-cavities during creep due to grain boundary sliding (i.e. creep cavitation)
- 2) Coupled with the precipitation of K-feldspar for progressively sealing the micro-cavities.

Accordingly, we termed this grain mixing process as the “cavitation-seal mechanism”. This mechanism explains the inter-grain phase mixing and the inhibition of grain growth due to pinning. The process that allows the transient cavitation during deformation is grain boundary sliding. However, the accommodation mechanisms involved during GBS were different for quartz and feldspars, being dislocation-accommodated GBS in quartz and diffusion-accommodated (dissolution-precipitation) GBS in feldspars. This different mode of GBS accommodation explains the difference in the grain shape between quartz and feldspar (e.g. Langdon, 2006).

The inter-grain mixing model depends strongly on both creep cavitation and potassium feldspar diffusivity. In our study case, the mixing model does not require quartz precipitation for grain size reduction or the mixing, in line with its lack of evidence during deformation. The model also agrees with ultramylonite features such as the highly irregular shapes of Kfs and the persistence of Kfs-rich bands. Despite this, other mineral phases might have a more efficient diffusivity at different conditions. Yet, little is known on the precipitation rates of Kfs or plagioclase at high pressures and moderate to high temperatures and even less on cavitation rates during deformation, both hindering the estimation of timescales required for an effective inter-grain mixing at a fixed strain rate.

Regarding the extension of this model to depths below the semi-brittle field, Kfs diffusivity seems to be rather irrespective of T and stress at Earth crust conditions, see for example the interpretation of similar Kfs microstructures at amphibolite facies in Berhmann and Mainprice (1987). In contrast, cavitation is theoretically very sensitive to confining pressure (Goetze criterion), limiting the extension of models that involve creep cavitation below middle crust conditions (but see Menegon et al. 2015). The cavitation-seal mechanism avoids volume expansion if dissolution-precipitation rates of the mobile phase/s are sufficiently efficient.

Acknowledgments

This work was supported by the Spanish Ministry of Economy and Competitiveness (MINECO) excellence research [grant numbers CGL2014-53388-P, CGL2010-14890], and by the Asturias Regional Government (Spain) [grant number BP07-120]. We thank Professor A. Marcos, who discovered the Penedo Gordo ultramylonite bands along with M. A. Lopez-Sanchez and assisted in the collection of samples, and Professor Francisco J. Martínez for their valuable discussions and suggestions in the field. A previous review by Andrew J. Cross provided us with some new important ideas. We thank the reviews by Jacques Précigout and John Platt for greatly improving the content in the manuscript and the editorial guidance of Philippe Agard.

References

- Akinfiyev, N.N., Diamond, L.W., 2009. A simple predictive model of quartz solubility in water–salt–CO₂ systems at temperatures up to 1000 °C and pressures up to 1000 MPa. *Geochim. Cosmochim. Acta* 73, 1597–1608. <https://doi.org/10.1016/J.GCA.2008.12.011>
- Austin, N.J., Evans, B., 2009. The kinetics of microstructural evolution during deformation of calcite. *J. Geophys. Res. Solid Earth* 114, B09402. <https://doi.org/10.1029/2008JB006138>
- Bachmann, F., Hielscher, R., Schaeben, H., 2010. Texture Analysis with MTEX – Free and Open Source Software Toolbox. *Solid State Phenom.* 160, 63–68. <https://doi.org/10.4028/www.scientific.net/SSP.160.63>
- Barnhoorn, A., Bystricky, M., Burlini, L., Kunze, K., 2004. The role of recrystallisation on the deformation behaviour of calcite rocks: large strain torsion experiments on Carrara marble. *J. Struct. Geol.* 26, 885–903. <https://doi.org/10.1016/j.jsg.2003.11.024>
- Barnhoorn, A., Bystricky, M., Kunze, K., Burlini, L., Burg, J.P., 2005. Strain localisation in biminerale rocks: Experimental deformation of synthetic calcite–anhydrite aggregates. *Earth Planet. Sci. Lett.* 240, 748–763. <https://doi.org/10.1016/j.epsl.2005.09.014>
- Bastida, F., Marcos, A., Marquínez, J., Martínez Catalán, J.R., Pérez-Estaún, A., Pulgar, J.A., 1984. Mapa Geológico de España e. 1:200.000 (La Coruña), Hoja no 1. Instituto Geológico y Minero de España, Madrid, España.
- Behr, W.M., Platt, J.P., 2014. Brittle faults are weak, yet the ductile middle crust is strong: Implications for lithospheric mechanics. *Geophys. Res. Lett.* 41, 8067–8075. <https://doi.org/10.1002/2014GL061349>
- Behrmann, J.H., 1985. Crystal plasticity and superplasticity in quartzite; A natural example. *Tectonophysics* 115, 101–129. [https://doi.org/10.1016/0040-1951\(85\)90102-7](https://doi.org/10.1016/0040-1951(85)90102-7)
- Behrmann, J.H., Mainprice, D., 1987. Deformation mechanisms in a high-temperature quartz-feldspar mylonite: evidence for superplastic flow in the lower continental crust. *Tectonophysics* 140, 297–305. [https://doi.org/10.1016/0040-1951\(87\)90236-8](https://doi.org/10.1016/0040-1951(87)90236-8)
- Bercovici, D., Ricard, Y., 2012. Mechanisms for the generation of plate tectonics by two-phase grain-damage and pinning. *Phys. Earth Planet. Inter.* 202–203, 27–55. <https://doi.org/10.1016/j.pepi.2012.05.003>

- Bercovici, D., Skemer, P., 2017. Grain damage, phase mixing and plate-boundary formation. *J. Geodyn.* <https://doi.org/10.1016/j.jog.2017.05.002>
- Bons, P.D., Urai, J.L., 1994. Experimental deformation of two-phase rock analogues. *Mater. Sci. Eng. A* 175, 221–229. [https://doi.org/10.1016/0921-5093\(94\)91061-8](https://doi.org/10.1016/0921-5093(94)91061-8)
- Boullier, A.M., Gueguen, Y., 1975. SP-Mylonites: Origin of some mylonites by superplastic flow. *Contrib. to Mineral. Petrol.* 50, 93–104. <https://doi.org/10.1007/BF00373329>
- Bourcier, M., Bornert, M., Dimanov, A., Héripré, E., Raphanel, J.L., 2013. Multiscale experimental investigation of crystal plasticity and grain boundary sliding in synthetic halite using digital image correlation. *J. Geophys. Res. Solid Earth* 118, 511–526. <https://doi.org/10.1002/jgrb.50065>
- Brodie, K.H., Rutter, E.H., 1987. The role of transiently fine-grained reaction products in syntectonic metamorphism: natural and experimental examples. *Can. J. Earth Sci.* 24, 556–564. <https://doi.org/10.1139/e87-054>
- Brudy, M., Zoback, M.D., Fuchs, K., Rummel, F., Baumgärtner, J., 1997. Estimation of the complete stress tensor to 8 km depth in the KTB scientific drill holes: Implications for crustal strength. *J. Geophys. Res. Solid Earth* 102, 18453–18475. <https://doi.org/10.1029/96JB02942>
- Bystricky, M., Kunze, K., Burlini, L., Burg, J.P., 2000. High Shear Strain of Olivine Aggregates: Rheological and Seismic Consequences. *Science* 290, 1564–1567. <https://doi.org/10.1126/science.290.5496.1564>
- Capdevila, R., 1969. Le métamorphisme régional progressif et les granites dans le segmentet hercynien Galice nord orientale (NW l'Espagne). Université de Montpellier, France.
- Clark, P.J., Evans, F.C., 1954. Distance to Nearest Neighbor as a Measure of Spatial Relationships in Populations. *Ecology* 35, 445–453. <https://doi.org/10.2307/1931034>
- Cross, A.J., Prior, D.J., Stipp, M., Kidder, S., 2017a. The recrystallized grain size piezometer for quartz: An EBSD-based calibration. *Geophys. Res. Lett.* 44, 6667–6674. <https://doi.org/10.1002/2017GL073836>
- Cross, A.J., Hirth, G., Prior, D.J., 2017b. Effects of secondary phases on crystallographic preferred orientations in mylonites. *Geology* 45, 955–958. <https://doi.org/10.1130/G38936.1>
- Cross, A.J., Skemer, P., 2017. Ultramylonite generation via phase mixing in high-strain experiments. *J. Geophys. Res. Solid Earth* 122, 1744–1759. <https://doi.org/10.1002/2016JB013801>

- Davis, J.C., 2002. *Statistics and data analysis in geology*. J. Wiley.
- De Bresser, J.H.P., Evans, B., Renner, J., 2002. On estimating the strength of calcite rocks under natural conditions. *Geol. Soc. London, Spec. Publ.* 200, 309–329.
<https://doi.org/10.1144/GSL.SP.2001.200.01.18>
- De Bresser, J.H.P., Ter Heege, J.H., Spiers, C.J., Ter Heege, J.H., Spiers, C.J., 2001. Grain size reduction by dynamic recrystallization: can it result in major rheological weakening? *Int. J. Earth Sci.* 90, 28–45. <https://doi.org/10.1007/s005310000149>
- Dell'Angelo, L.N., Tullis, J., 1996. Textural and mechanical evolution with progressive strain in experimentally deformed aplite. *Tectonophysics* 256, 57–82. [https://doi.org/10.1016/0040-1951\(95\)00166-2](https://doi.org/10.1016/0040-1951(95)00166-2)
- den Brok, B., Zahid, M., Passchier, C., 1998. Cataclastic solution creep of very soluble brittle salt as a rock analogue. *Earth Planet. Sci. Lett.* 163, 83–95. [https://doi.org/10.1016/S0012-821X\(98\)00177-0](https://doi.org/10.1016/S0012-821X(98)00177-0)
- Derby, B., Ashby, M.F., 1987. On dynamic recrystallization. *Scr. Metall.* 21, 879–884.
[https://doi.org/10.1016/0036-9748\(87\)90341-3](https://doi.org/10.1016/0036-9748(87)90341-3)
- Dimanov, A., Rybacki, E., Wirth, R., Dresen, G., 2007. Creep and strain-dependent microstructures of synthetic anorthite–diopside aggregates. *J. Struct. Geol.* 29, 1049–1069.
<https://doi.org/10.1016/J.JSG.2007.02.010>
- Edmond, J.M., Paterson, M.S., 1972. Volume changes during the deformation of rocks at high pressures. *Int. J. Rock Mech. Min. Sci. Geomech. Abstr.* 9, 161–182.
[https://doi.org/10.1016/0148-9062\(72\)90019-8](https://doi.org/10.1016/0148-9062(72)90019-8)
- Evans, K., 2007. Quartz solubility in salt-bearing solutions at pressures to 1 GPa and temperatures to 900°C. *Geofluids* 7, 451–467. <https://doi.org/10.1111/j.1468-8123.2007.00199.x>
- Evans, B., Kohlstedt, D.L., 1995. Rheology of rocks, in: *Rock Physics & Phase Relations: A Handbook of Physical Constants*. American Geophysical Union, pp. 148–165.
<https://doi.org/10.1029/RF003p0148>
- Fitz-Gerald, J.D., Stünitz, H., 1993. Deformation of granitoids at low metamorphic grade I: Reactions and grain size reduction. *Tectonophysics* 221, 269–297.
[https://doi.org/10.1016/0040-1951\(93\)90163-E](https://doi.org/10.1016/0040-1951(93)90163-E)

- Fliervoet, T.F., White, S.H., Drury, M.R., 1997. Evidence for dominant grain-boundary sliding deformation in greenschist- and amphibolite-grade polymineralic ultramylonites from the Redbank Deformed Zone, Central Australia. *J. Struct. Geol.* 19, 1495–1520. [https://doi.org/10.1016/S0191-8141\(97\)00076-X](https://doi.org/10.1016/S0191-8141(97)00076-X)
- Fukuda, J., Okudaira, T., 2013. Grain-size-sensitive creep of plagioclase accompanied by solution–precipitation and mass transfer under mid-crustal conditions. *J. Struct. Geol.* 51, 61–73. <https://doi.org/10.1016/j.jsg.2013.03.006>
- Fukuda, J., Okudaira, T., Satsukawa, T., Michibayashi, K., 2012. Solution–precipitation of K-feldspar in deformed granitoids and its relationship to the distribution of water. *Tectonophysics* 532, 175–185. <https://doi.org/10.1016/j.tecto.2012.01.033>
- Fusseis, F., Regenauer-Lieb, K., Liu, J., Hough, R.M., De Carlo, F., 2009. Creep cavitation can establish a dynamic granular fluid pump in ductile shear zones. *Nature* 459, 974–7. <https://doi.org/10.1038/nature08051>
- Géraud, Y., Caron, J., Faure, P., 1995. Porosity network of a ductile shear zone. *J. Struct. Geol.* 17, 1757–1769. [https://doi.org/10.1016/0191-8141\(95\)00067-N](https://doi.org/10.1016/0191-8141(95)00067-N)
- Gifkins, R.C., 1978. Grain rearrangements during superplastic deformation. *J. Mater. Sci.* 13, 1926–1936. <https://doi.org/10.1007/BF00552899>
- Gilgannon, J., Fusseis, F., Menegon, L., Regenauer-Lieb, K., Buckman, J., 2017. Hierarchical creep cavity formation in an ultramylonite and implications for phase mixing. *Solid Earth* 8, 1193–1209. <https://doi.org/10.5194/se-8-1193-2017>
- Gleason, G.C., Tullis, J., 1995. A flow law for dislocation creep of quartz aggregates determined with the molten salt cell. *Tectonophysics* 247, 1–23. [https://doi.org/10.1016/0040-1951\(95\)00011-B](https://doi.org/10.1016/0040-1951(95)00011-B)
- González-Lodeiro, F., Hernández-Urroz, J., Klein, E., Martínez Catalán, J.R., 1981. Mapa Geológico de España e. 1:200.000 (Lugo), Hoja no 8. Instituto Geológico y Minero de España, Madrid, España.
- Green, N.L., Usdansky, S.I., 1986. Ternary-feldspar mixing relations and thermobarometry. *Am. Mineral.* 71, 1100–1108.
- Handy, M.R., 1994. Flow laws for rocks containing two non-linear viscous phases: A phenomenological approach. *J. Struct. Geol.* 16, 287–301. [https://doi.org/10.1016/0191-8141\(94\)90035-3](https://doi.org/10.1016/0191-8141(94)90035-3)

- Handy, M.R., 1990. The solid-state flow of polymineralic rocks. *J. Geophys. Res.* 95, 8647.
<https://doi.org/10.1029/JB095iB06p08647>
- Hansen, L.N., Zimmerman, M.E., Kohlstedt, D.L., 2011. Grain boundary sliding in San Carlos olivine: Flow law parameters and crystallographic-preferred orientation. *J. Geophys. Res.* 116, B08201. <https://doi.org/10.1029/2011JB008220>
- Hertz, P., 1909. Über den gegenseitigen durchschnittlichen Abstand von Punkten, die mit bekannter mittlerer Dichte im Raume angeordnet sind. *Math. Ann.* 67, 387–398.
<https://doi.org/10.1007/BF01450410>
- Herwegh, M., Linckens, J., Ebert, A., Berger, A., Brodhag, S.H., 2011. The role of second phases for controlling microstructural evolution in polymineralic rocks: A review. *J. Struct. Geol.* 33, 1728–1750. <https://doi.org/10.1016/j.jsg.2011.08.011>
- Hidas, K., Tommasi, A., Garrido, C.J., Padrón-Navarta, J.A., Mainprice, D., Vauchez, A., Barou, F., Marchesi, C., 2016. Fluid-assisted strain localization in the shallow subcontinental lithospheric mantle. *Lithos* 262, 636–650. <https://doi.org/10.1016/j.lithos.2016.07.038>
- Hippertt, J.F., 1998. Breakdown of feldspar, volume gain and lateral mass transfer during mylonitization of granitoid in a low metamorphic grade shear zone. *J. Struct. Geol.* 20, 175–193. [https://doi.org/10.1016/S0191-8141\(97\)00083-7](https://doi.org/10.1016/S0191-8141(97)00083-7)
- Hiraga, T., Miyazaki, T., Yoshida, H., Zimmerman, M.E., 2013. Comparison of microstructures in superplastically deformed synthetic materials and natural mylonites: Mineral aggregation via grain boundary sliding. *Geology* 41, 959–962. <https://doi.org/10.1130/G34407.1>
- Hirth, G., Kohlstedt, D.L., 1995. Experimental constraints on the dynamics of the partially molten upper mantle: 2. Deformation in the dislocation creep regime. *J. Geophys. Res. Solid Earth* 100, 15441–15449. <https://doi.org/10.1029/95JB01292>
- Hirth, G., Tullis, J., 1992. Dislocation creep regimes in quartz aggregates. *J. Struct. Geol.* 14, 145–159. [https://doi.org/10.1016/0191-8141\(92\)90053-Y](https://doi.org/10.1016/0191-8141(92)90053-Y)
- Holdaway, M.J., 1971. Stability of andalusite and the aluminum silicate phase diagram. *Am. J. Sci.* 271, 97–131. <https://doi.org/10.2475/ajs.271.2.97>
- Holdaway, M.J., Mukhopadhyay, B., 1993. A reevaluation of the stability relations of andalusite; thermochemical data and phase diagram for the aluminum silicates. *Am. Mineral.* 78, 298–315.

- Hövelmann, J., Putnis, A., Geisler, T., Schmidt, B.C., Golla-Schindler, U., 2009. The replacement of plagioclase feldspars by albite: observations from hydrothermal experiments. *Contrib. to Mineral. Petrol.* 159, 43–59. <https://doi.org/10.1007/s00410-009-0415-4>
- Ishii, K., Kanagawa, K., Shigematsu, N., Okudaira, T., 2007. High ductility of K-feldspar and development of granitic banded ultramylonite in the Ryoke metamorphic belt, SW Japan. *J. Struct. Geol.* 29, 1083–1098. <https://doi.org/10.1016/j.jsg.2007.02.008>
- Jerram, D.A., Cheadle, M.J., Hunter, R.H., Elliott, M.T., 1996. The spatial distribution of grains and crystals in rocks. *Contrib. to Mineral. Petrol.* 125, 60–74. <https://doi.org/10.1007/s004100050206>
- Jiang, H., Lee, C.-T.A., Morgan, J.K., Ross, C.H., 2015. Geochemistry and thermodynamics of an earthquake: A case study of pseudotachylites within mylonitic granitoid. *Earth Planet. Sci. Lett.* 430, 235–248. <https://doi.org/10.1016/j.epsl.2015.08.027>
- Jiang, J., Lapusta, N., 2016. Deeper penetration of large earthquakes on seismically quiescent faults. *Science (80-.)*. 352, 1293–1297. <https://doi.org/10.1126/science.aaf1496>
- Jin, D., Karato, S., Obata, M., 1998. Mechanisms of shear localization in the continental lithosphere: inference from the deformation microstructures of peridotites from the Ivrea zone, northwestern Italy. *J. Struct. Geol.* 20, 195–209. [https://doi.org/10.1016/S0191-8141\(97\)00059-X](https://doi.org/10.1016/S0191-8141(97)00059-X)
- Kidder, S., Avouac, J.-P., Chan, Y.-C., 2012. Constraints from rocks in the Taiwan orogen on crustal stress levels and rheology. *J. Geophys. Res. Solid Earth* 117, B09408. <https://doi.org/10.1029/2012JB009303>
- Kilian, R., Heilbronner, R., Stünitz, H., 2011. Quartz grain size reduction in a granitoid rock and the transition from dislocation to diffusion creep. *J. Struct. Geol.* 33, 1265–1284. <https://doi.org/10.1016/j.jsg.2011.05.004>
- Kirby, S.H., 1985. Rock mechanics observations pertinent to the rheology of the continental lithosphere and the localization of strain along shear zones. *Tectonophysics* 119, 1–27. [https://doi.org/10.1016/0040-1951\(85\)90030-7](https://doi.org/10.1016/0040-1951(85)90030-7)
- Kirkpatrick, J.D., Rowe, C.D., 2013. Disappearing ink: How pseudotachylites are lost from the rock record. *J. Struct. Geol.* 52, 183–198. <https://doi.org/10.1016/j.jsg.2013.03.003>

- Kohlstedt, D.L., Evans, B., Mackwell, S.J., 1995. Strength of the lithosphere: Constraints imposed by laboratory experiments. *J. Geophys. Res.* 100, 17587–17602.
<https://doi.org/10.1029/95JB01460>
- Krabbendam, M., Urai, J.L., van Vliet, L.J., 2003. Grain size stabilisation by dispersed graphite in a high-grade quartz mylonite: an example from Naxos (Greece). *J. Struct. Geol.* 25, 855–866.
[https://doi.org/10.1016/S0191-8141\(02\)00086-X](https://doi.org/10.1016/S0191-8141(02)00086-X)
- Kretz, R., 1983. Symbols for rock-forming minerals. *Am. Mineral.* 68.
- Kretz, R., 1969. On the spatial distribution of crystals in rocks. *Lithos* 2, 39–65.
[https://doi.org/10.1016/S0024-4937\(69\)80005-8](https://doi.org/10.1016/S0024-4937(69)80005-8)
- Kruhl, J.H., 2003. Prism- and basal-plane parallel subgrain boundaries in quartz: a microstructural geothermobarometer. *J. Metamorph. Geol.* 14, 581–589. <https://doi.org/10.1046/j.1525-1314.1996.00413.x>
- Langdon, T.G., 2006. Grain boundary sliding revisited: Developments in sliding over four decades. *J. Mater. Sci.* 41, 597–609. <https://doi.org/10.1007/s10853-006-6476-0>
- Linckens, J., Bruijn, R., Skemer, P., 2014. Dynamic recrystallization and phase mixing in experimentally deformed peridotite. *Earth Planet. Sci. Lett.* 388, 134–142.
<https://doi.org/10.1016/j.epsl.2013.11.037>
- Linckens, J., Herwegh, M., Müntener, O., Mercolli, I., 2011. Evolution of a polymineralic mantle shear zone and the role of second phases in the localization of deformation. *J. Geophys. Res.* 116, B06210. <https://doi.org/10.1029/2010JB008119>
- Lloyd, G.E., 1987. Atomic Number and Crystallographic Contrast Images with the SEM: A Review of Backscattered Electron Techniques. *Mineral. Mag.* 51, 3–19.
<https://doi.org/10.1180/minmag.1987.051.359.02>
- Lopez-Sanchez, M.A., 2017. GrainSizeTools script. figshare.
<https://doi.org/10.6084/m9.figshare.1383130.v13>
- Lopez-Sanchez, M.A., 2013. Análisis tectónico de la Falla de Vivero (Galicia, NO de España). Universidad de Oviedo. <http://hdl.handle.net/10651/20282>
- Lopez-Sanchez, M.A., Llana-Fúnez, S., 2016. An extension of the Saltykov method to quantify 3D grain size distributions in mylonites. *J. Struct. Geol.* 93, 149–161.
<https://doi.org/10.1016/j.jsg.2016.10.008>

- Lopez-Sanchez, M.A., Llana-Fúnez, S., 2015. An evaluation of different measures of dynamically recrystallized grain size for paleopiezometry or paleowattometry studies. *Solid Earth* 6, 475–495. <https://doi.org/10.5194/se-6-475-2015>
- Lopez-Sanchez, M.A., Marcos, A., Martínez, F.J., Iriondo, A., Llana-Fúnez, S., 2015. Setting new constraints on the age of crustal-scale extensional shear zone (Vivero fault): implications for the evolution of Variscan orogeny in the Iberian massif. *Int. J. Earth Sci.* 104, 927–962. <https://doi.org/10.1007/s00531-014-1119-1>
- Maddock, R.H., 1992. Effects of lithology, cataclasis and melting on the composition of fault-generated pseudotachylytes in Lewisian gneiss, Scotland. *Tectonophysics* 204, 261–278. [https://doi.org/10.1016/0040-1951\(92\)90311-S](https://doi.org/10.1016/0040-1951(92)90311-S)
- Mainprice, D., Bachmann, F., Hielscher, R., Schaeben, H., 2014. Descriptive tools for the analysis of texture projects with large datasets using MTEX : strength, symmetry and components. *Geol. Soc. London, Spec. Publ.* 409, 251–271. <https://doi.org/10.1144/SP409.8>
- Mancktelow, N.S., Pennacchioni, G., 2005. The control of precursor brittle fracture and fluid–rock interaction on the development of single and paired ductile shear zones. *J. Struct. Geol.* 27, 645–661. <https://doi.org/10.1016/j.jsg.2004.12.001>
- Manning, C.E., 1994. The solubility of quartz in H₂O in the lower crust and upper mantle. *Geochim. Cosmochim. Acta* 58, 4831–4839. [https://doi.org/10.1016/0016-7037\(94\)90214-3](https://doi.org/10.1016/0016-7037(94)90214-3)
- Marcos, A., 2013. Un nuevo mapa geológico de la parte septentrional del Domo de Lugo (Galicia oriental, NO de España): Implicaciones sobre la estratigrafía, estructura y evolución tectónica del Manto de Mondoñedo. *Trab. Geol.* 33, 171–200.
- Martínez, F.J., Carreras, J., Arboleya, M.L., Dietsch, C., 1996. Structural and metamorphic evidence of local extension along the Vivero fault coeval with bulk crustal shortening in the Variscan chain (NW Spain). *J. Struct. Geol.* 18, 61–73. [https://doi.org/10.1016/0191-8141\(95\)00080-W](https://doi.org/10.1016/0191-8141(95)00080-W)
- Martínez, F.J., Reche, J., Arboleya, M.L., 2001. P-T modelling of the andalusite-kyanite-andalusite sequence and related assemblages in high-Al graphitic pelites. Prograde and retrograde paths in a late kyanite belt in the Variscan Iberia. *J. Metamorph. Geol.* 19, 661–677. <https://doi.org/10.1046/j.0263-4929.2001.00335.x>
- Martínez Catalán, J.R., 1985. Estratigrafía y estructura del domo de Lugo (sector oeste de la zona Asturoccidental-leonesa). *Corpus Geologicum Gallaeciae Segunda serie II*. La Coruña.

- Matte, P., 1968. La structure de la virgation hercynienne de Galice (Espagne). *Geol. Alp.* 44, 157–280.
- Menegon, L., Füsseis, F., Stünitz, H., Xiao, X., 2015. Creep cavitation bands control porosity and fluid flow in lower crustal shear zones. *Geology* 43, 227–230.
<https://doi.org/10.1130/G36307.1>
- Menegon, L., Pennacchioni, G., Spiess, R., 2008. Dissolution-precipitation creep of K-feldspar in mid-crustal granite mylonites. *J. Struct. Geol.* 30, 565–579.
<https://doi.org/10.1016/j.jsg.2008.02.001>
- Miranda, E.A., Hirth, G., John, B.E., 2016. Microstructural evidence for the transition from dislocation creep to dislocation-accommodated grain boundary sliding in naturally deformed plagioclase. *J. Struct. Geol.* 92, 30–45. <https://doi.org/10.1016/j.jsg.2016.09.002>
- Moecher, D.P., Sharp, Z.D., 2004. Stable isotope and chemical systematics of pseudotachylyte and wall rock, Homestake shear zone, Colorado, USA: Meteoric fluid or rock-buffered conditions during coseismic fusion? *J. Geophys. Res.* 109, B12206.
<https://doi.org/10.1029/2004JB003045>
- Newton, R.C., Manning, C.E., 2000. Quartz solubility in H₂O-NaCl and H₂O-CO₂ solutions at deep crust-upper mantle pressures and temperatures: 2–15 kbar and 500–900°C. *Geochim. Cosmochim. Acta* 64, 2993–3005. [https://doi.org/10.1016/S0016-7037\(00\)00402-6](https://doi.org/10.1016/S0016-7037(00)00402-6)
- Oliphant, T.E., 2007. Python for Scientific Computing. *Comput. Sci. Eng.* 9, 10–20.
<https://doi.org/10.1109/MCSE.2007.58>
- Ortega, L.A., Gil-Ibarguchi, J.I., 1990. The genesis of late Hercynian granitoids from Galicia (northwestern Spain): Inferences from REE studies. *J. Geol.* 98, 189–211.
- Parga-Pondal, I., Matte, P., Capdevila, R., Parga, J.R., Teixeira, C., Floor, P., 1967. Carte géologique du Nord-ouest de la Peninsule Ibérique (Hercynien et ante-hercynien). e. 1:500.000. Direcção Geral de Minas e Serviços Geológicos de Portugal. Lisboa.
- Passchier, C.W., Trouw, R.A.J., 2005. *Microtectonics* (2nd edition), second. ed. Springer-Verlag Berlin Heidelberg.
- Pattison, D.R.M., 1992. Stability of Andalusite and Sillimanite and the Al_2SiO_5 Triple Point: Constraints from the Ballachulish Aureole, Scotland. *J. Geol.* 100, 423–446.
<https://doi.org/10.1086/629596>

- Pearce, M.A., Wheeler, J., 2011. Grain growth and the lifetime of diffusion creep deformation. *Geol. Soc. London, Spec. Publ.* 360, 257–272. <https://doi.org/10.1144/SP360.15>
- Pec, M., Stünitz, H., Heilbronner, R., Drury, M.R., 2016. Semi-brittle flow of granitoid fault rocks in experiments. *J. Geophys. Res. Solid Earth* 121, 1677–1705. <https://doi.org/10.1002/2015JB012513>
- Pennacchioni, G., 2005. Control of the geometry of precursor brittle structures on the type of ductile shear zone in the Adamello tonalites, Southern Alps (Italy). *J. Struct. Geol.* 27, 627–644. <https://doi.org/10.1016/j.jsg.2004.11.008>
- Pieri, M., Burlini, L., Kunze, K., Stretton, I., Olgaard, D.L., 2001. Rheological and microstructural evolution of Carrara marble with high shear strain: results from high temperature torsion experiments. *J. Struct. Geol.* 23, 1393–1413. [https://doi.org/10.1016/S0191-8141\(01\)00006-2](https://doi.org/10.1016/S0191-8141(01)00006-2)
- Pilling, J., Ridley, N., 1989. *Superplasticity in crystalline solids*. Institute of Metals, London.
- Platt, J.P., 2015. Rheology of two-phase systems: A microphysical and observational approach. *J. Struct. Geol.* 77, 213–227. <https://doi.org/10.1016/j.jsg.2015.05.003>
- Platt, J.P., Behr, W.M., 2011. Grainsize evolution in ductile shear zones: Implications for strain localization and the strength of the lithosphere. *J. Struct. Geol.* 33, 537–550. <https://doi.org/10.1016/j.jsg.2011.01.018>
- Précigout, J., Prigent, C., Palasse, L., Pochon, A., 2017. Water pumping in mantle shear zones. *Nat. Commun.* 8, 15736. <https://doi.org/10.1038/ncomms15736>
- Price, N.A., Johnson, S.E., Gerbi, C.C., West, D.P., 2012. Identifying deformed pseudotachylite and its influence on the strength and evolution of a crustal shear zone at the base of the seismogenic zone. *Tectonophysics* 518–521, 63–83. <https://doi.org/10.1016/j.tecto.2011.11.011>
- Putnis, A., John, T., 2010. Replacement Processes in the Earth's Crust. *Elements* 6, 159–164. <https://doi.org/10.2113/gselements.6.3.159>
- Ramsay, J.G., 1980. Shear zone geometry: A review. *J. Struct. Geol.* 2, 83–99. [https://doi.org/10.1016/0191-8141\(80\)90038-3](https://doi.org/10.1016/0191-8141(80)90038-3)
- Reber, J.E., Lavier, L.L., Hayman, N.W., 2015. Experimental demonstration of a semi-brittle origin for crustal strain transients. *Nat. Geosci.* 8, 712–715. <https://doi.org/10.1038/ngeo2496>
- Reche, J., Martínez, F.J., Arboleya, M.L., 1998a. Low- to medium-pressure Variscan metamorphism in Galicia (NW Spain): evolution of a kyanite-bearing synform and associated bounding

antiformal domains. *Geol. Soc. London, Spec. Publ.* 138, 61–79.

<https://doi.org/10.1144/GSL.SP.1996.138.01.05>

Reche, J., Martínez, F.J., Arboleya, M.L., Dietsch, C., Briggs, W.D., 1998b. Evolution of a kyanite-bearing belt within a HT-LP orogen: the case of NW Variscan Iberia. *J. Metamorph. Geol.* 16, 379–394. <https://doi.org/10.1111/j.1525-1314.1998.00142.x>

Ree, J.-H., 1994. Grain boundary sliding and development of grain boundary openings in experimentally deformed octachloropropane. *J. Struct. Geol.* 16, 403–418.

[https://doi.org/10.1016/0191-8141\(94\)90044-2](https://doi.org/10.1016/0191-8141(94)90044-2)

Ree, J.-H., Kim, H., Han, R., Jung, H., 2005. Grain-size reduction of feldspars by fracturing and neocrystallization in a low-grade granitic mylonite and its rheological effect. *Tectonophysics* 407, 227–237. <https://doi.org/10.1016/j.tecto.2005.07.010>

Reed, M.G., Howard, C. V., 1997. Edge-corrected estimators of the nearest-neighbour distance distribution function for three-dimensional point patterns. *J. Microsc.* 186, 177–184.

<https://doi.org/10.1046/j.1365-2818.1997.1710741.x>

Rogowitz, A., White, J.C., Grasemann, B., 2016. Strain localization in ultramylonitic marbles by simultaneous activation of dislocation motion and grain boundary sliding (Syros, Greece). *Solid Earth* 7, 355–366. <https://doi.org/10.5194/se-7-355-2016>

Rueden, C.T., Schindelin, J., Hiner, M.C., DeZonia, B.E., Walter, A.E., Eliceiri, K.W., 2017. ImageJ2: ImageJ for the next generation of scientific image data. *arXiv* 1701.05940.

Rutter, E.H., Brodie, K.H., 1988. The role of tectonic grain size reduction in the rheological stratification of the lithosphere. *Geol. Rundschau* 77, 295–307.

<https://doi.org/10.1007/BF01848691>

Rutter, E.H., Brodie, K.H., 1992. The rheology of the lower continental crust. In: Fountain, D., Arculus, R., Kay, R. (Eds.), *Continental Lower Crust*, Elsevier Series on Developments in Geodynamics, pp. 201–268.

Rutter, E.H., Casey, M., Burlini, L., 1994. Preferred crystallographic orientation development during the plastic and superplastic flow of calcite rocks. *J. Struct. Geol.* 16, 1431–1446.

[https://doi.org/10.1016/0191-8141\(94\)90007-8](https://doi.org/10.1016/0191-8141(94)90007-8)

Rybacki, E., Wirth, R., Dresen, G., 2008. High-strain creep of feldspar rocks: Implications for cavitation and ductile failure in the lower crust. *Geophys. Res. Lett.* 35, L04304.

<https://doi.org/10.1029/2007GL032478>

- Schmid, S.M., Boland, J.N., Paterson, M.S., 1977. Superplastic flow in finegrained limestone. *Tectonophysics* 43, 257–291. [https://doi.org/10.1016/0040-1951\(77\)90120-2](https://doi.org/10.1016/0040-1951(77)90120-2)
- Scholz, C.H., 2002. *The Mechanics of Earthquakes and Faulting*, 2nd ed. Cambridge University Press.
- Scholz, C.H., 1988. The brittle-plastic transition and the depth of seismic faulting. *Geol. Rundschau* 77, 319–328. <https://doi.org/10.1007/BF01848693>
- Schwarz, H., Exner, H.E., 1983. The characterization of the arrangement of feature centroids in planes and volumes. *J. Microsc.* 129, 155–169. <https://doi.org/10.1111/j.1365-2818.1983.tb04170.x>
- Scott, D.W., 1992. *Multivariate Density Estimation: Theory, Practice, and Visualization*. John Wiley & Sons, New York, Chichester.
- Segall, P., Simpson, C., 1986. Nucleation of ductile shear zones on dilatant fractures. *Geology* 14, 56. [https://doi.org/10.1130/0091-7613\(1986\)14<56:NODSZO>2.0.CO;2](https://doi.org/10.1130/0091-7613(1986)14<56:NODSZO>2.0.CO;2)
- Shimizu, I., 1998. Stress and temperature dependence of recrystallized grain size: A subgrain misorientation model. *Geophys. Res. Lett.* 25, 4237. <https://doi.org/10.1029/1998GL900136>
- Shmulovich, K.I., Yardley, B.W.D., Graham, C.M., 2006. Solubility of quartz in crustal fluids: experiments and general equations for salt solutions and H₂O-CO₂ mixtures at 400-800°C and 0.1-0.9 GPa. *Geofluids* 6, 154–167. <https://doi.org/10.1111/j.1468-8123.2006.00140.x>
- Skemer, P., Katayama, I., Jiang, Z., Karato, S., 2005. The misorientation index: Development of a new method for calculating the strength of lattice-preferred orientation. *Tectonophysics* 411, 157–167. <https://doi.org/10.1016/j.tecto.2005.08.023>
- Stipp, M., Tullis, J., 2003. The recrystallized grain size piezometer for quartz. *Geophys. Res. Lett.* 30, 1–5. <https://doi.org/10.1029/2003GL018444>
- Stünitz, H., Fitz-Gerald, J.D., 1993. Deformation of granitoids at low metamorphic grade. II: Granular flow in albite-rich mylonites. *Tectonophysics* 221, 299–324. [https://doi.org/10.1016/0040-1951\(93\)90164-F](https://doi.org/10.1016/0040-1951(93)90164-F)
- Stünitz, H., Tullis, J., 2001. Weakening and strain localization produced by syn-deformational reaction of plagioclase. *Int. J. Earth Sci.* 90, 136–148. <https://doi.org/10.1007/s005310000148>

- Sullivan, W.A., Boyd, A.S., Monz, M.E., 2013. Strain localization in homogeneous granite near the brittle–ductile transition: A case study of the Kellyland fault zone, Maine, USA. *J. Struct. Geol.* 56, 70–88. <https://doi.org/10.1016/j.jsg.2013.09.003>
- Sundberg, M., Cooper, R.F., 2008. Crystallographic preferred orientation produced by diffusional creep of harzburgite: Effects of chemical interactions among phases during plastic flow. *J. Geophys. Res.* 113, B12208. <https://doi.org/10.1029/2008JB005618>
- Takagi, H., Goto, K., Shigematsu, N., 2000. Ultramylonite bands derived from cataclasite and pseudotachylyte in granites, northeast Japan. *J. Struct. Geol.* 22, 1325–1339. [https://doi.org/10.1016/S0191-8141\(00\)00034-1](https://doi.org/10.1016/S0191-8141(00)00034-1)
- Tasaka, M., Zimmerman, M.E., Kohlstedt, D.L., 2017a. Rheological Weakening of Olivine + Orthopyroxene Aggregates Due to Phase Mixing: 1. Mechanical Behavior. *J. Geophys. Res. Solid Earth* 122, 7584–7596. <https://doi.org/10.1002/2017JB014333>
- Tasaka, M., Zimmerman, M.E., Kohlstedt, D.L., Stünitz, H., Heilbronner, R., 2017b. Rheological Weakening of Olivine + Orthopyroxene Aggregates Due To Phase Mixing: Part 2. Microstructural Development. *J. Geophys. Res. Solid Earth* 122, 7597–7612. <https://doi.org/10.1002/2017JB014311>
- Trepmann, C.A., Stöckhert, B., 2013. Short-wavelength undulatory extinction in quartz recording coseismic deformation in the middle crust - an experimental study. *Solid Earth* 4, 263–276. <https://doi.org/10.5194/se-4-263-2013>
- Trepmann, C.A., Stöckhert, B., Dorner, D., Moghadam, R.H., Küster, M., Röller, K., 2007. Simulating coseismic deformation of quartz in the middle crust and fabric evolution during postseismic stress relaxation - An experimental study. *Tectonophysics* 442, 83–104. <https://doi.org/10.1016/j.tecto.2007.05.005>
- Tukey, J.W., 1977. *Exploratory data analysis*, Series in Behavioral Science: Quantitative Methods, Reading. Addison-Wesley Educational Publishers Inc.
- Tullis, J., Yund, R.A., 1987. Transition from cataclastic flow to dislocation creep of feldspar: Mechanisms and microstructures. *Geology* 15, 606. [https://doi.org/10.1130/0091-7613\(1987\)15<606:TFCFTD>2.0.CO;2](https://doi.org/10.1130/0091-7613(1987)15<606:TFCFTD>2.0.CO;2)
- Twiss, R.J., Moores, E.M., 2007. *Structural Geology*, Second Edi. ed, Geology. W. H. Freeman.
- U.S. GEOLOGICAL SURVEY, 2004. *A compilation of rate parameters of water-mineral interaction kinetics for application to geochemical modeling*. Menlo Park, California.

- Vauchez, A., Tommasi, A., Mainprice, D., 2012. Faults (shear zones) in the Earth's mantle. *Tectonophysics* 558, 1–27. <https://doi.org/10.1016/j.tecto.2012.06.006>
- Viegas, G., Menegon, L., Archanjo, C., 2016. Brittle grain-size reduction of feldspar, phase mixing and strain localization in granitoids at mid-crustal conditions (Pernambuco shear zone, NE Brazil). *Solid Earth* 7, 375–396. <https://doi.org/10.5194/se-7-375-2016>
- Walker, A.N., Rutter, E.H., Brodie, K.H., 1990. Experimental study of grain-size sensitive flow of synthetic, hot-pressed calcite rocks. *Geol. Soc. London, Spec. Publ.* 54, 259–284. <https://doi.org/10.1144/GSL.SP.1990.054.01.24>
- Warren, J.M., Hirth, G., 2006. Grain size sensitive deformation mechanisms in naturally deformed peridotites. *Earth Planet. Sci. Lett.* 248, 438–450. <https://doi.org/10.1016/j.epsl.2006.06.006>
- Wheeler, J., 2009. The preservation of seismic anisotropy in the Earth's mantle during diffusion creep. *Geophys. J. Int.* 178, 1723–1732. <https://doi.org/10.1111/j.1365-246X.2009.04241.x>
- White, S.H., Knipe, R.J., 1978. Transformation- and reaction-enhanced ductility in rocks. *J. Geol. Soc. London.* 135, 513–516. <https://doi.org/10.1144/gsjgs.135.5.0513>
- Wright, S.I., Nowell, M.M., Field, D.P., 2011. A Review of Strain Analysis Using Electron Backscatter Diffraction. *Microsc. Microanal.* 17, 316–329. <https://doi.org/10.1017/S1431927611000055>

Figure captions

Fig. 1. (a) The Iberian massif in the Iberian Peninsula. (b) Geological map around the Penedo Gordo granite. (c) Simplified cross-section.

Fig. 2. An aspect of Penedo Gordo granite in the field and on polished hand specimens with different degrees of deformation. (a) Deformed facies in the field, developing synthetic ultramylonite bands (white arrows). (b) Granite with no apparent signs of deformation microstructures with the unaided eye (Grade I). (c) Grain segmentation of main phases portrayed in false colour to estimate the modal quantities. Blue – quartz, Pink – feldspars, and black - biotite (d) Granite with quartz showing a faint shape fabric (Grade II). (e) Granite showing feldspar fracturing (Grade III) and the formation of a micro shear zone enriched in very fine-grained biotite. (f) Sample alternating fine-grained highly deformed zones (grey colour) with zones with a high modal fraction of feldspar porphyroclasts (Grade IV). (g) Homogeneous ultramylonite sample. The whitening around the edges is due to sericitic alteration. Scale bars in hand specimens are 1 cm in length.

Fig. 3. Solid-state deformation microstructures in low-strain granite samples. (a) Blocky sub-grains in quartz. (b) Irregular grain boundaries in quartz with examples of bulging. (c) Irregular quartz-quartz grain boundary showing new very fine strain-free quartz grains along them. (d) K-feldspar with flame-perthite mainly nucleated at grain boundaries and fractures without apparent offset. (e) General development of flame-perthites in K-feldspar following two principal planes. In the lower part, a fracture without offset shows very small grains along with it. (f) Detail of flame-perthite. (g) Irregular grain boundary between two feldspar grains in contact. Note the presence of some new very-fine feldspar grains. (h) Oligoclase grain showing micro-fractures and sub-grain boundary development. (i) Myrmekite in plagioclase. All micrographs with crossed polars.

Fig. 4. Quartz deformation features in mylonite samples (MAL-05). (a) Quartz grain with strings of recrystallized grains in continuity with the adjacent feldspar fractures (indicated with arrows). (b) Quartz grain with several parallel strings of recrystallized grains. The orientation of these strings is similar to the orientation of the main fracture in the feldspar located below. (c) Example of dynamic recrystallization in quartz cutting across a distorted blocky sub-grain structure. (d, e) Mylonite image

mosaic (d) and phase map (e) showing a complete dynamic recrystallization and the connection of quartz aggregates due to accumulated strain. (f) Band contrast and crystallographic orientation overlaying image of dynamically recrystallized quartz. Apparent mean grain size is 35.8 μm (linear scale). Step size is 1 μm in EBSD maps. Below, inverse pole figures showing the orientation colour scheme and density of distribution in z-direction. (g) Grain orientation spread (GOS) in degrees for each reconstructed grain. (h) Distribution of GOS using a kernel density estimator. The location of percentiles 95 and 99 are indicated. The inset shows the distribution of GOS within the 99% percentile.

Fig. 5. Comparison of quartz microstructures in mylonites and ultramylonites. Median (solid lines) and mean (dashed lines) are indicated. (a) Apparent grain size distribution in mylonites (DRX quartz) and ultramylonites (dispersed matrix quartz). (b) Volume-weighted cumulative distribution for recrystallized quartz. In the inset, detail for the grain sizes equal to or less than 30 microns. (c, d) Derived lognormal shape (MSD value) of the 3D grain size distribution using the two-step method (Lopez-Sanchez and Llana-Fúnez, 2016) for DRX quartz (c) and dispersed quartz (d). (e) Distribution of grain aspect ratios. (f) Morphological roughness (solidity) of grains.

Fig. 6. Evolution of quartz crystallographic-preferred orientation (CPO) from mylonites to ultramylonites. To the left, point-per-grain pole figures with CPO distribution for [c] and <a>-axes. To the right, uncorrelated misorientation distribution (M-index). Note that the intensity of the CPO maxima, indicated by vertical bars, changes notably between the different pole figures. Pole figures are upper hemisphere equal-area projections. Half-width values for the estimation of the J index were 7.5, 9.4, and 19, respectively. The number of grains referred to as n.

Fig. 7. Feldspar deformation microstructures in mylonites (sample MAL-05). (a) Optical micrograph in crossed polars of a K-feldspar grain showing two dominant fracture planes. (b) Optical micrograph in crossed polars showing the internal microstructure of a Kfs grain with undulose extinction and fracturing. (c) BSE image of conjugate fracture planes in Kfs where albite crystallizes in Kfs fractures whereas Kfs in oligoclase grains. (d) Detail of fracture planes in a partly albitized Kfs. The albitization (dark grey) evolves from the fracture surface to the inner grain. Dashed lines indicate the reaction fronts. In the lower half, some new very-fine albite grains appear. Flame-like dark grey features within the Kfs grains are flame perthites. (e) Detail of a fracture plane in Kfs filled

by an almost pure mosaic of very fine albite grains. This is the most common aspect of Kfs fractures. To the left, some flame perthites appear. (f) Detail of a fracture plane in Kfs but in this case, the amount of Kfs fragments within the fracture is notable. (g) Optical micrograph (crossed polars) showing two feldspar grains fractured; oligoclase at the top and Kfs at the bottom. The oligoclase grain shows a dirty appearance due to sericitic alteration and the presence of biotite along fractures. (h) Fracture plane in oligoclase filled with biotite and Kfs. Sericite is absent along the fractures. Kfs fills the porosity generated in oligoclase grains. (i) Fracture plane in oligoclase filled with Kfs. Note that there is no mosaic of small grains filling the fracture, but a mixture of irregular Kfs grains filling the space. A network of small-scale fractures affects the entire oligoclase grain. (j) Example of Kfs filling cavities in a quartz-oligoclase contact as well as inside the oligoclase grain. (k) Dark biotite-enriched vein with breccia. (l) The composition of the parent and new feldspar grains. Mineral symbols after Kretz (1983).

Fig. 8. SEM-BSE micrographs highlighting the microstructure in ultramylonites (sample MAL-07). Quartz appears as dark grey, albite medium dark grey (very similar to quartz), Kfs as light grey, and biotite as white. (a) Three well-differentiated domains inherited from the mylonite development. Ultramylonite bands evolve to a homogeneous mixture of the three main phases (for examples see compositional and SEM maps in the supplementary material). (b) The apparent grain size of quartz grains below the tip of a quartz pod, the ones surrounded by the Kfs, is notably smaller compared to quartz within the pods. (c, d) Quartz pod tip (c) and boundary (d) showing Kfs and Bt precipitation at triple junctions and between the quartz grains detached from the pod. White arrows point to Kfs grains with highly irregular shapes, sometimes showing necking structures, due to filling irregular cavities. (e) The gradual isolation of quartz grains towards the Kfs-rich band at the upper right indicates the progressive disaggregation of quartz pods and the movement of quartz grains towards the Kfs-rich band. (f) An aspect of the well-mixed ultramylonite matrix. In the upper right corner, a close-up of the area marked showing Kfs grains with a typical film-like shape. Note that in contrast to other mineral phases albite grain boundaries always appear thickened or pitted. Also note that in contrast to feldspar, quartz grains appear as near-equant grains and rather polygonal.

Fig. 9. Shape and grain size features of different mineral phases within the polymineralic well-mixed matrix. Median (solid line) and mean (dashed line) are indicated. (a) Apparent grain size distributions. (b) Aspect ratios. (c) Morphological roughness (solidity).

Fig. 10. Spatial analysis of quartz grains in ultramylonites. (a) SEM-BSE image mosaic showing the distribution of quartz grains (in blue) within the ultramylonite matrix (thin section MAL-07). (b) A density map of quartz grain centroids (white dots) calculated using a 2D Kernel Density Estimate with a bandwidth based on Scott's rule (Scott, 1992) reveals subtle density differences in the selected area. Still, it is possible to detect a density band arranged parallel to the tectonic foliation, likely related to the disintegration of an old quartz aggregate. (c) Comparison between the empirical and theoretical (Poisson) nearest-neighbour distance distribution using probability mass (left) and cumulative distribution (right) charts.

Fig. 11. Schematic diagram illustrating the sequence of steps in the disGBS inter-grain mixing model for quartz. Partially adapted from Gifkins (1978) and Pilling and Ridley (1989). (a) Initial arrangement of four perfectly hexagonal and uniform grains. (b, c) Evolution without grain rotation. If grains preserve their shape, micro-cavities appear after a small amount of grain sliding; thin gaps between grains and small pockets at triple junctions (b). Voids seal as soon as they open by precipitation of secondary phases (mainly Kfs in our case study). With evolution, Kfs develop necking or highly irregular shapes (c). (d, e) Evolving microstructure involving sliding plus grain rotation. Large rotations are necessary to lose or weaken pre-existing CPOs and require equant or near-equant grains. Overcoming the locking at grain corners (indicated by arrows in (e) requires the deformation of grain mantles by dislocation creep. (f) Grain boundaries adjust to reach dihedral angles. Different grain sizes and shapes, neither perfectly hexagonal nor uniform, occur in crystalline aggregates, and some grains may be decreasing in size during deformation due to dynamic recrystallization and/or dissolution. In addition, this is a two-dimensional model and actual sliding and rotation can occur in directions not contained in the represented section. Hence, this model attempts a rough but fair approximation of the phenomena occurred during GBS.

Fig. 12. Schematic diagram illustrating the opening of transient pull-apart micro-cavities during the sliding of feldspar grains in the extension direction. Extension direction is horizontal. This is coupled with fluid infiltration and the progressive sealing of Kfs during ultramylonite band formation. The sequence is somewhat similar to the sequence a-b-c-f shown in figure 11. The elongated appearance of feldspars excludes major grain rotations during the sliding due to the locking between grains. The cavitation-seal mechanism produces the inter-grain mixing of albite and Kfs destroying the albite-

rich bands. In contrast, it produces larger aspect ratios in the Kfs grains (*cf.* figure 5 in Langdon, 2006) without breaking down the Kfs-rich bands. Lateral displacements of adjacent grains towards the pull-apart cavities are the main mechanism for the inter-grain mixing in Kfs-rich bands.

Fig. 13. Zone with alternating Kfs and quartz-rich bands traced by green lines. Quartz-rich layers are in fact quartz + Kfs mixtures since Kfs precipitation is everywhere destroying the original quartz-rich layers. In contrast, Kfs-rich bands remain mostly made up of Kfs with some albite and biotite grains. Highlighted in red, the only quartz grains visible within the Kfs-rich bands. Note that the size of such quartz grains is similar to those observed in the Qtz + Kfs layers.

Table 1. *Compilation of Deformation Microstructures and Deformation Mechanisms in Granitoids deformed in the semi-brittle field*

References	Protonic ^a	Environment conditions	Microstructures			Ultramylonite bands ^b	New mica	Deformation mechanisms	Compositional changes
			quartz	K-feldspar	plagioclase				
Fitz-Gerald and Stünitz (1993), Stünitz and Fitz-Gerald (1993)	Granites from Corvatsch, Le Châtelard (both located in Switzerland), and Wyangala (SE Australia).	Lower to upper greenschist facies. Le Châtelard (T~250 °C); Corvatsch (T~300-400 °C); Wyangala (upper greenschist)	SGR-type dynamic recrystallization. No CPO data.	Fracturing. Rarely myrmekite or perthites. Crystallization of albite along fractures and rims.	Fracturing. Crystallization of albite along fractures and rims.	Qtz-Alb-mica-Ep	Chl, Bt or Ms (depends on the granite)	Qtz: dislocation creep;	no data
						GS: 3-30 micron		Felds: cataclasis + dissolution-precipitation creep;	
						CPO: no data		ultramylonites: GBS accommodated by diffusion creep	
						SPO: no data			
Hippert (1998)	Granitic rocks (Moeda Bonfim shear zone; Quadrilátero Ferrífero, SE Brazil). Kfs+Pl+Qtz+Bt	Upper greenschist facies T~400-450 °C P~400 MPa	SGR-type dynamic recrystallization & CPO (dominant prisms <a> slip)	Fracturing and development of flame perthite (An ₅₋₁₂)	Fracturing. Crystallization of Ep+Ms+Qtz aggregates in fractures.	No data	Ms, minor quantities of Bt and Chl	Qtz: dislocation creep; Felds: cataclasis + dissolution-precipitation creep	Increase in K, depletion in Ca and Na. General enrichment in Muscovite.
Ree et al. (2005)	Granite (Yecheon shear zone, South Korea) Kfs+Qtz+Pl+Ms (±Bt)	Greenschist facies T~300-400 °C P~300 MPa	SGR-type dynamic recrystallization & CPO (dominant prisms and rhombs <a> slip)	Fracturing & myrmekite development. Crystallization of albite (An ₄₋₁₀) in fractures, although also Qtz, Ms or Chl.	Fracturing. Precipitation of Kfs in voids and fractures and, occasionally, Ms or Qtz.	Alb+Kfs+Ms+Qtz	Ms + minor Chl	Qtz: dislocation creep;	Increase in Ca, depletion in K. Enrichment in Ms. 25% less in feldspar.
						GS: 10-30 micron		Felds: cataclasis + dissolution-precipitation creep;	
						CPO: Alb (random)		ultramylonites: GBS accommodated by diffusion creep	
						SPO: no data			
Ishii et al. (2007)	Mizuma granodiorite (Konoyama mylonite zone, Ryoke belt,	Upper greenschist facies	SGR-type dynamic recrystallization & CPO (dominant prisms <a> slip)	Fracturing. Myrmekite is common but localized. Crystallization of	Fracturing. Crystallization of Qtz+Ep+Kfs+Bt aggregates in fractures.	Kfs+Pl+Qtz+Bt	Bt	Qtz: dislocation creep; Felds: cataclasis + dissolution-precipitation	No large differences in modal proportions of major constituent

	Japan). Qtz+Pl+Kfs+Bt (±Hb)			Qtz ± Kfs, Ep or Calcite in fractures.				on creep;	minerals . Kfs & Pl slightly decrease with deforma tion.
						CPO: Kfs (moderate)		ultramylonites: diffusion creep (Kfs show dislocation creep within the Kfs-rich bands)	
						SPO: nearly equant			
Menegon et al. (2008), Kilian et al. (2011)	Granodiorite (Gran Paradiso nappe, NW Alps, Italy). Kfs _(32%) +Pl _(27%) +Qtz _(27%) +Bt _(13%)	Lower amphibolite facies T~450-500 °C P~600-700 MPa	GBM-type dynamic recrystallization & CPO (dominant basal <a> slip)	Fracturing and myrmekite. Crystallization of Kfs (mainly), Pl and Ms along fractures and rims	Fracturing . Crystallization of Pl + Ms + Ep (±Grt) along fractures and rims.	Qtz- Kfs+Pl+Bt GS: 20-65 micron CPO: Qtz (random), Kfs (weak) SPO: Qtz (weak), Pl & Kfs (moderate)	Bt + Ms	Qtz: dislocation creep; Felds: cataclasis + dissolution- precipitation creep; ultramylonites: diffusion creep plus minor GBS	No data on bulk composition. Quartz modal quantity remains stable during deformation.
Fukuda et al. (2012), Fukuda and Okudaira (2013)	Deformed granitoids (Kawai mylonite zone, Ryoke belt, Japan). Qtz+Pl+Kfs+Bt	Upper greenschist to lower amphibolite facies T~400-500 °C	GBM-type (SGR-type in ultramylonites?) dynamic recrystallization & CPO (dominant prisms <a> slip)	Fracturing & flame perthite development. Crystallization of Kfs (mainly) and Pl along fractures and rims, both with random CPO.	Fracturing . Crystallization of Pl (from An20-40 to An23- 25) in fractures and rims (without CPO).	Qtz+Kfs+Pl±Chl GS: 8 micron (mean) CPO: Qtz (strong), Pl & Kfs (random) SPO: Qtz (weak), Pl & Kfs (strong)	Chl	Qtz: dislocation creep; Felds: cataclasis + dissolution- precipitation creep; ultramylonites: grain-size sensitive creep	Mass gain and loss during deformation. Increase in Fe, Mn, Mg and Ca. Depletion in K.
Sullivan et al. (2013)	Deblois granite (Kellyland fault zone, Maine, USA) Kfs + Qtz + Pl + Bt (±Hb)	Deformation started at amphibolite facies and finished at middle to lower greenschist facies	SGR-type dynamic recrystallization. Neoblast strings. Minor fractures. No CPO data.	Patchy undulose extinction , fracturing, myrmekite and perthite development. Crystallization of Kfs	Patchy undulose extinction and fracturing. Precipitation of Kfs and occasionally Bt in voids and fractures.	Kfs+Pl+Bt +Qtz GS: 1-10 micron CPO: no data	Bt	Qtz: dislocation creep; Felds: cataclasis + dissolution- precipitation creep; ultramylonites: GBS	Not detectable changes in the bulk composition of major, minor and REE

				and rarely Bt+Qtz in fractures.		SPO: no data		accommodated by diffusion creep	
Viegas et al. (2016)	Mylonitic monzogranite (Pernambuco Shear Zone, Brazil) with equal proportions of Qtz-Kfs-Pl(\pm Bt)	Lower amphibolite facies T~500-550 °C P~450-500 MPa	Dynamic recrystallization & CPO (dominant prisms <a> slip, minor rhomb <a> slip)	Fracturing . Rarely myrmekite. Crystallization of albite and Kfs along fractures and rims.	Fracturing . Crystallization of albite and Kfs along fractures and rims.	Qtz+Kfs+Pl	No	Qtz: dislocation creep;	No data on bulk composition. Feldspars do not change composition.
						GS: ~3.5 micron (mean)		Felds: cataclasis + dissolution-precipitation creep;	
						CPO: Kfs & Pl (random), Qtz (very weak)		ultramylonites: GBS accommodated by diffusion creep	
						SPO: subequant shapes			

^aPhases in relative abundance. *Qtz* - quartz, *Pl* - plagioclase, *Alb* - albite, *Kfs* - K-feldspar, *Bt* - biotite, *Chl* - chlorite, *Ms* - muscovite, *Ep* - epidote, *Hb* - hornblende.

^bGS - apparent grain size, CPO - crystallographic-preferred orientation, SPO - shape-preferred orientation

Table 2. *Apparent Grain Size and Grain Shape Parameters*

Phase	Size	Apparent grain size measures (μm)					Aspect Ratio			Solidity		
		Mean	SD (1s)	Median	IQR	KDE peak ^b	Mean	Median	IQR	Mean	Median	IQR
Qtz (mylonites)	1229 8	35.7 9 ^a	17.85	32.82	24.0 3	27.16	1.53	1.45	0.3 6	0.94	0.95	0.0 3
Qtz (matrix)	581	5.91	2.46	5.65	3.2	4.9	1.46	1.41	0.2 9	0.95	0.96	0.0 3
Kfs (matrix)	1009	4.26	2.47	3.76	2.74	2.98	1.97	1.89	0.7	0.92	0.94	0.0 6
albite (matrix)	426	3.33	1.48	3.07	2.49	2.49	1.82	1.75	0.6	0.93	0.94	0.0 4

^aAs indicated in Stipp and Tullis (2003), the RMS mean grain size (39.99 μm) was used to apply the piezometric relation

^bFrequency peak grain size according to a Gaussian Kernel Density Estimator (Lopez-Sanchez and Llana-Fúnez, 2015)

Table 3. *Results of CPO Strength Indexes*

EBSD map	Area (μm)	Step size (μm)	n	Min. area ^a	J-index	M-index
Qtz mylonite	1244x1660	1	572	---	2.90	0.092
Qtz pod 1	780x780	2	267	6	1.50	0.022
Qtz pod 2	780x390	1	266	5.2	2.60	0.083
Qtz pod 3	140*560	0.5	75	4.5	2.08	0.030
Qtz matrix	420x140	0.5	582	---	1.17	0.006

Note. The ODF model was estimated using the de la Vallée Poussin kernel as put in the MTEX matlab toolbox



^aMinimum grain profile area (μm^2) considered for recrystallized grains in the EBSD maps

Highlights:


- We propose a cavitation-seal mechanism for grain mixing during ultramylonitization
- Grain boundary sliding account for the opening of transient micro-cavities
- Potassium feldspar diffusivity and precipitation for sealing the cavities
- Diffusion- and dislocation-accommodated grain boundary sliding coexist (Fsp vs Qtz)

ROCK DOMAINS



Hangingwall sequence

-  **Silurian.** *Ampelites (Llagarinos Fm.) and an upper unit with slates, quartzites, and limestone lenses.*
-  **Ordovician sequence.** *Montes beds (Low Ord.), Armorican quartzite (Floian), Rubiana Fm., Luarca slates s.l. (Mid Ord.), and quartzites and slates (Upper Ord.).*
-  **Ollo de Sapo Fm.:** *Metamorphosed volcano-sedimentary, subvolcanic, and volcanic rocks. Age: Late Cambrian to Early Ordovician. a - coarse-grained facies*
-  **Undifferentiated nodulose schists**

Footwall sequence (Lugo dome)

-  **Ediacaran-Cambrian sequence:** *Quartzites, micaschist with calc-silicate beds, para- and orthogneisses, and migmatitic gneisses.*

Variscan granitoids

-  Two-mica leucogranites (S-type)
-  Calc-alkaline granitoids (I-type)

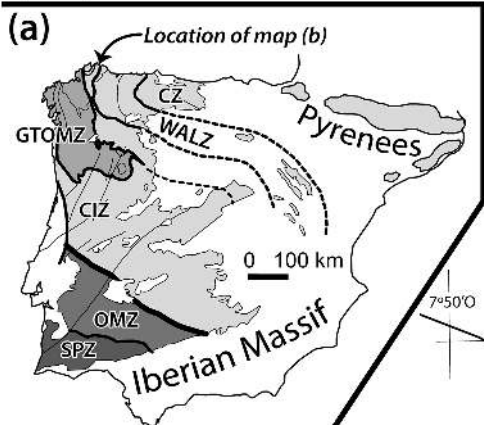
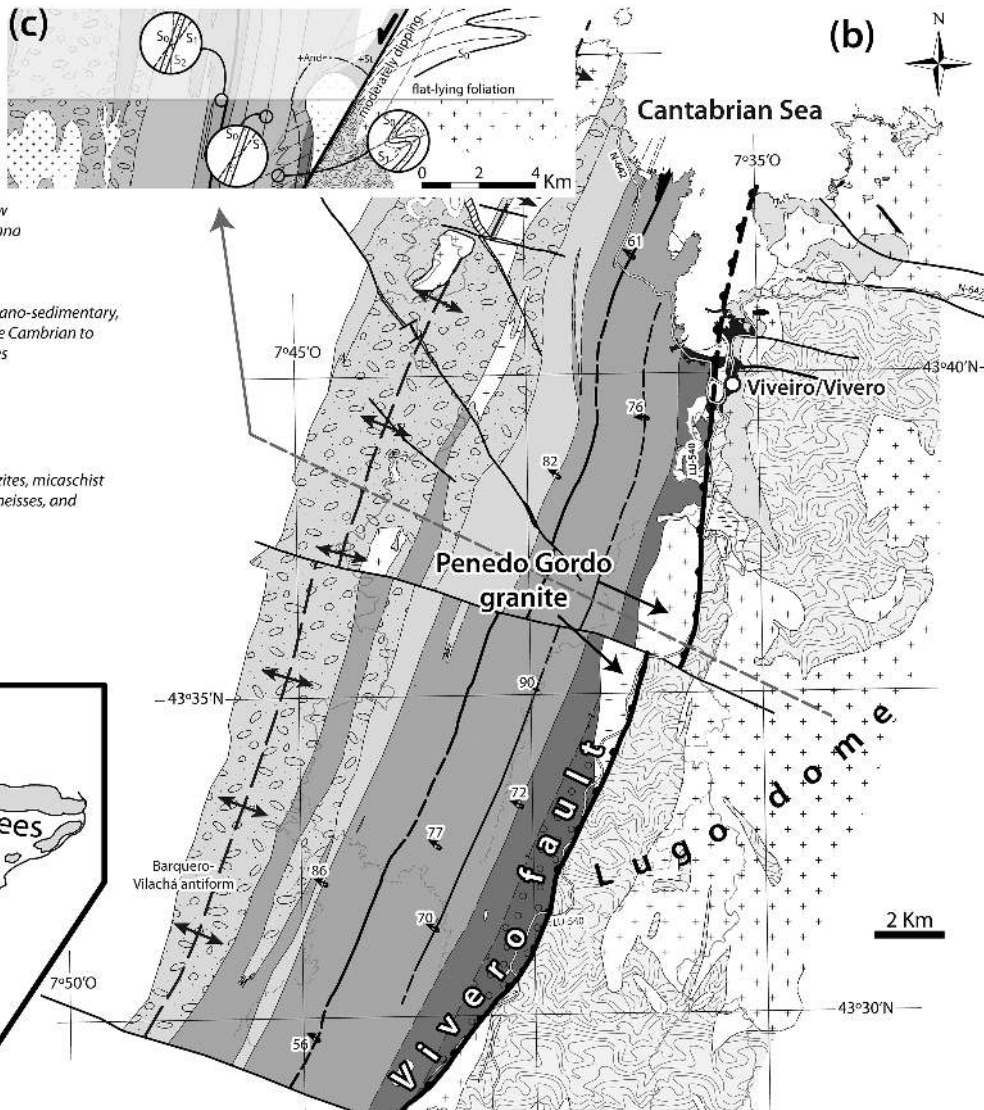


Figure 1

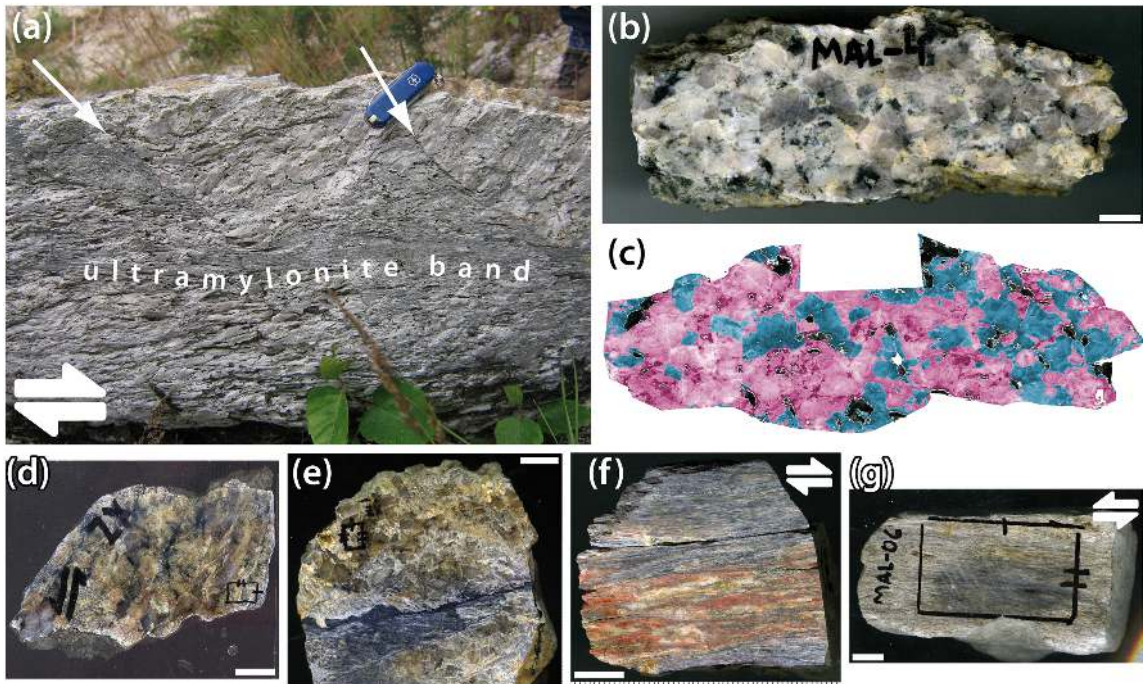


Figure 2

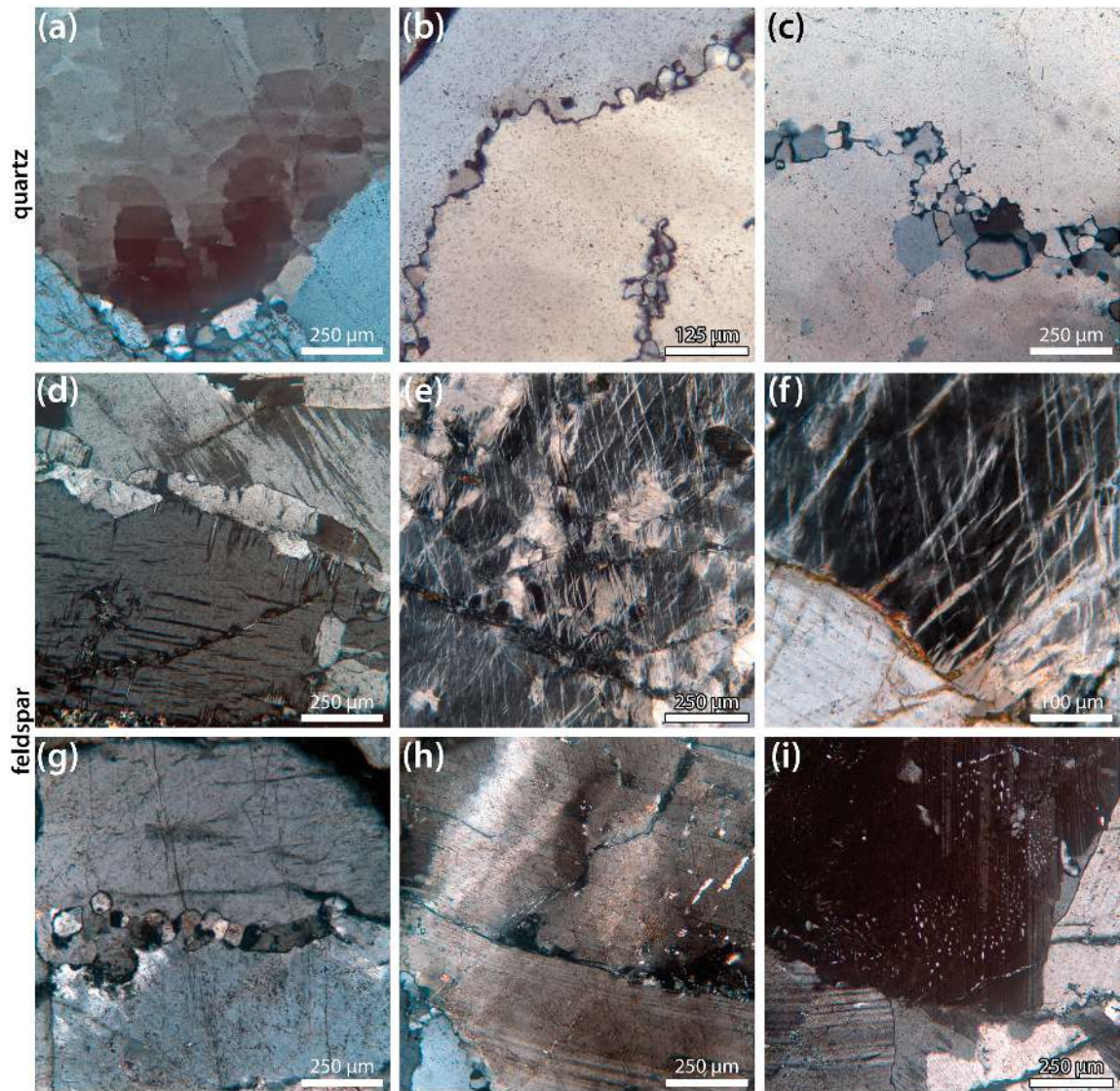


Figure 3

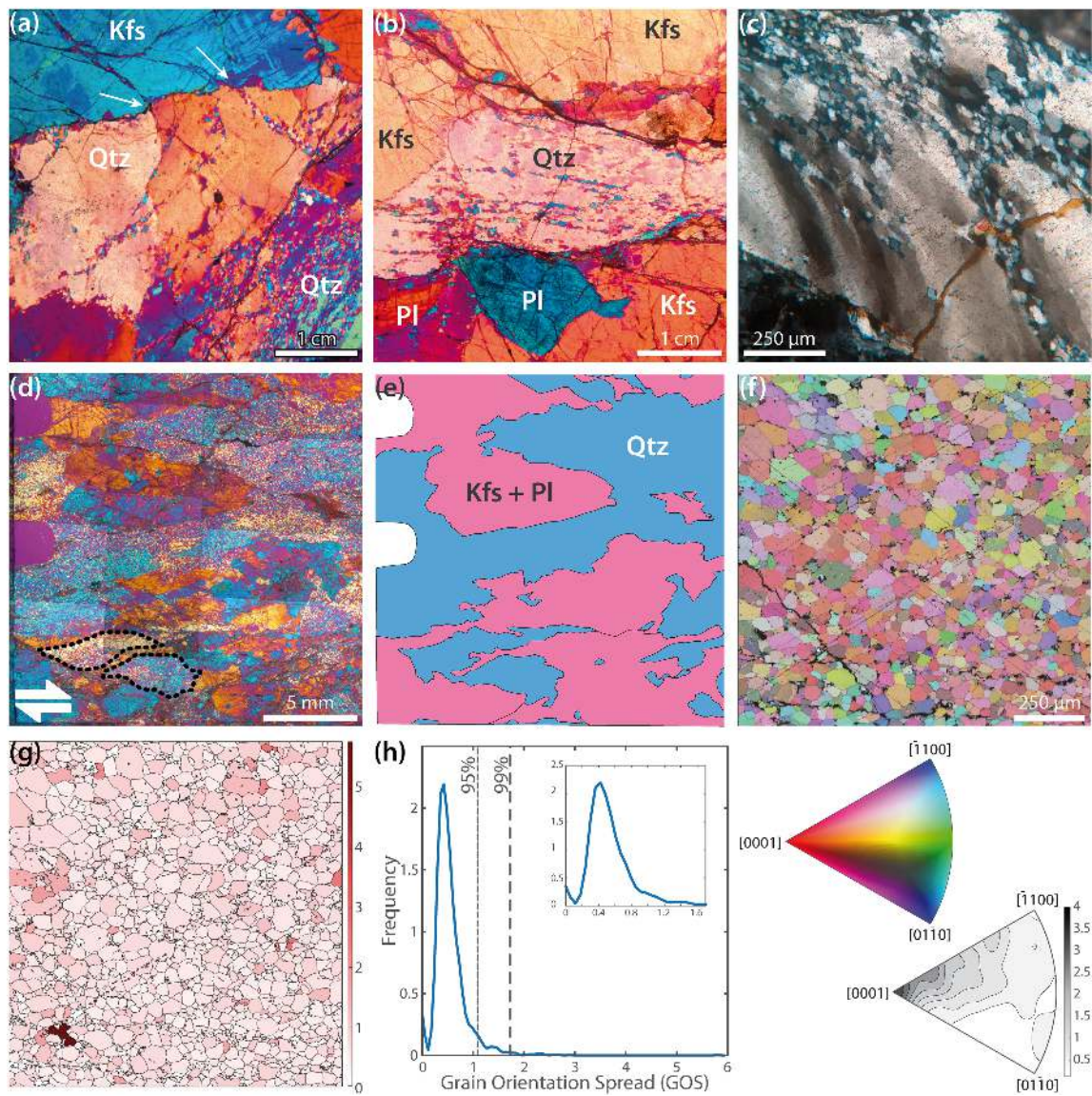


Figure 4

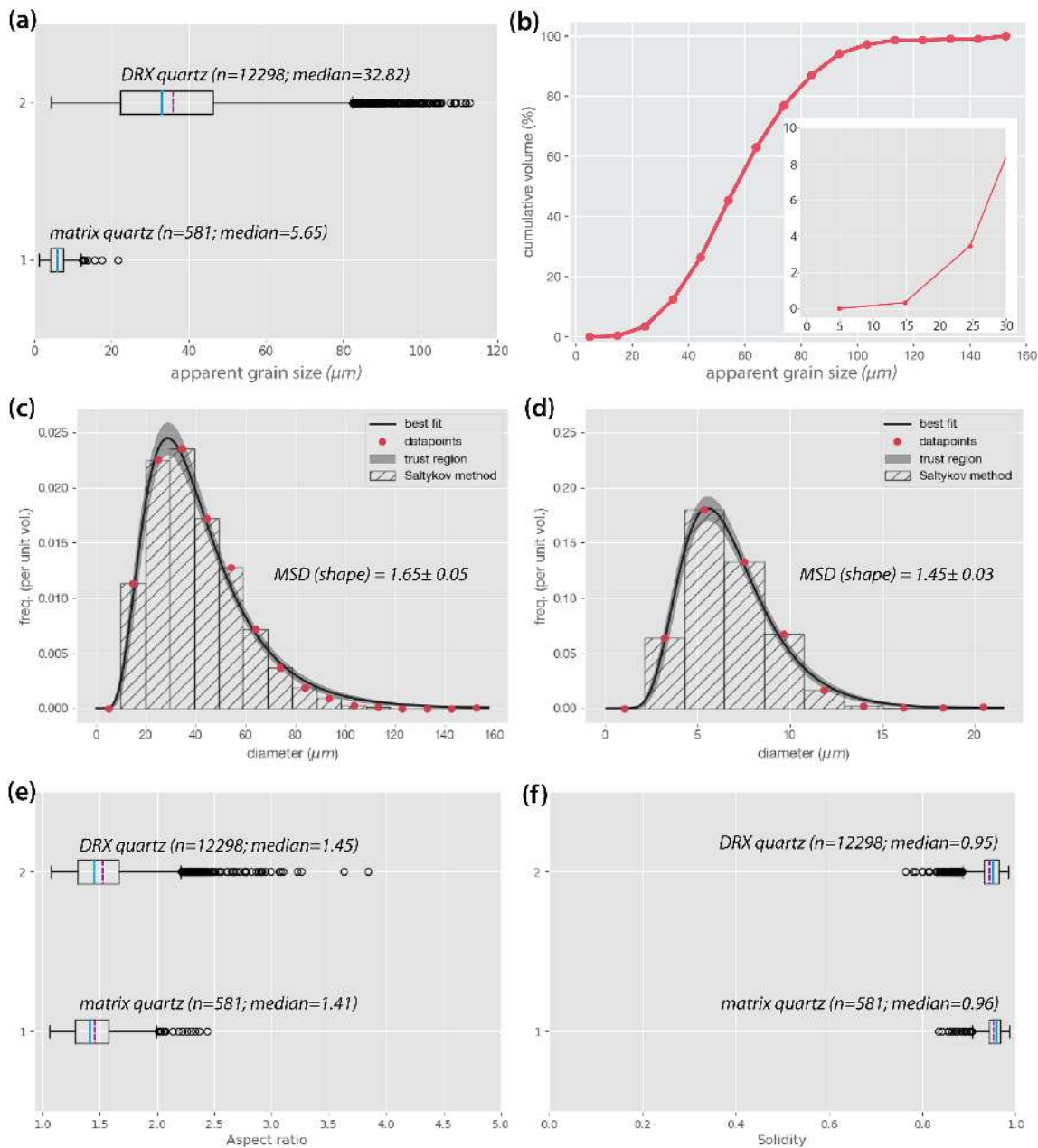
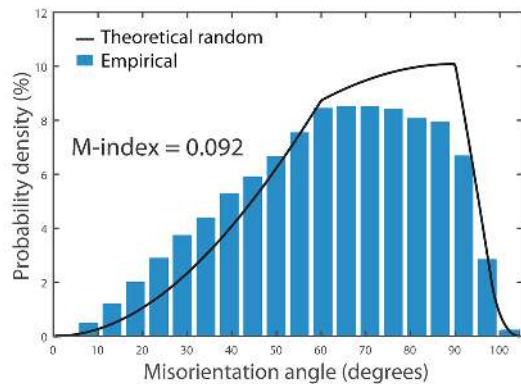
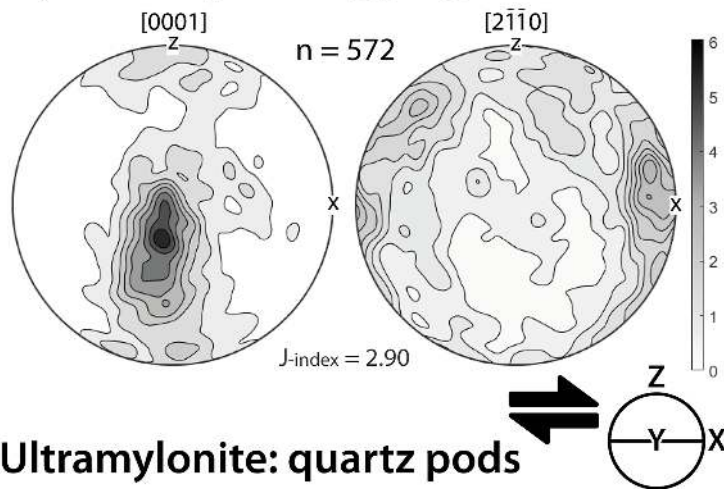
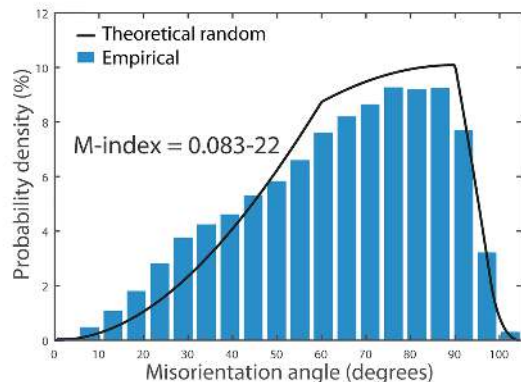
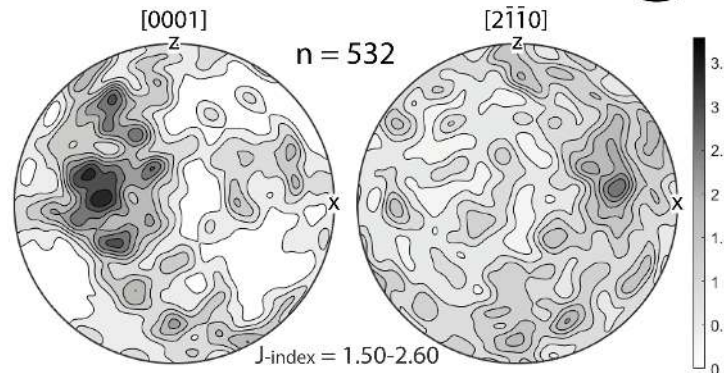


Figure 5

Mylonite: quartz aggregates



Ultramylonite: quartz pods



Ultramylonite: dispersed quartz

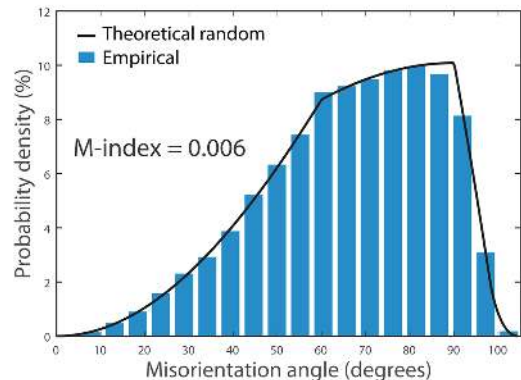
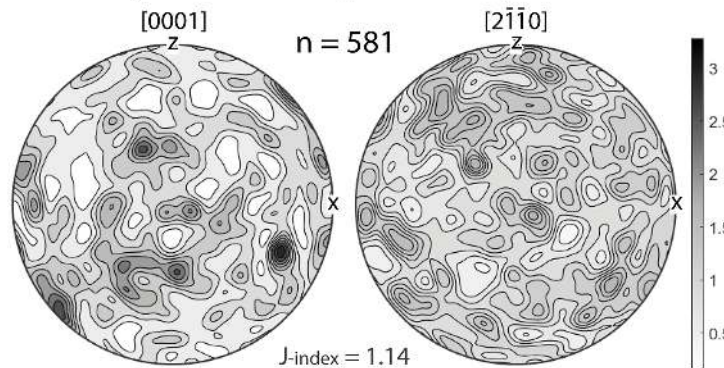


Figure 6

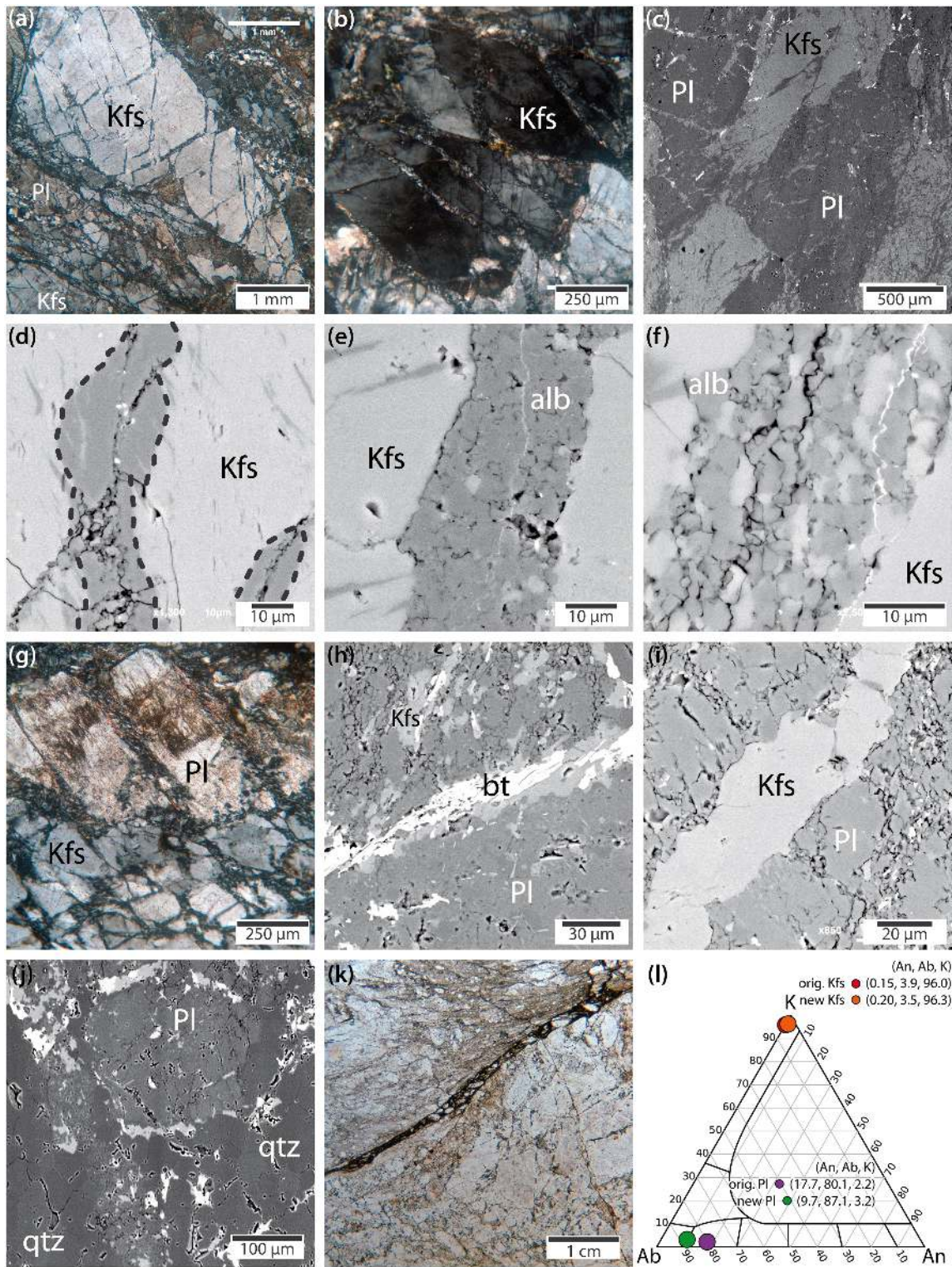


Figure 7

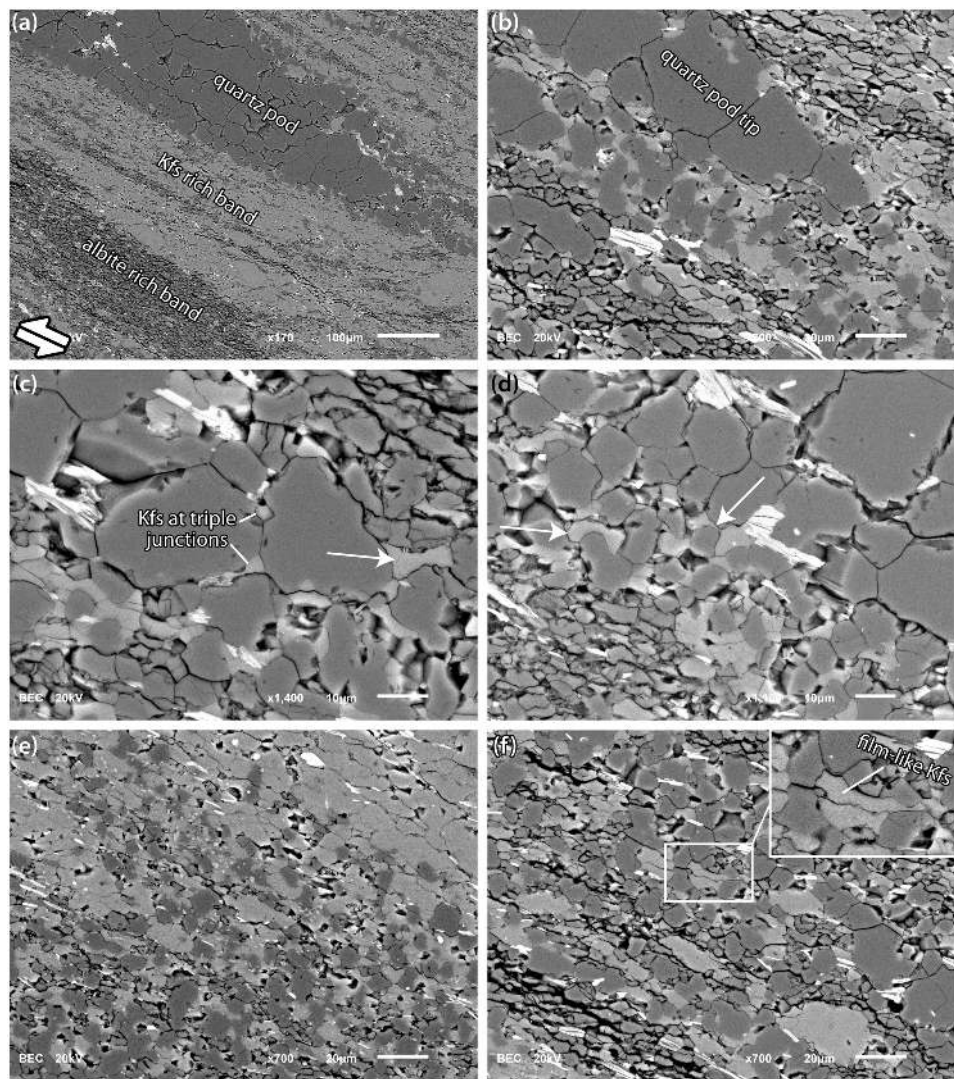


Figure 8

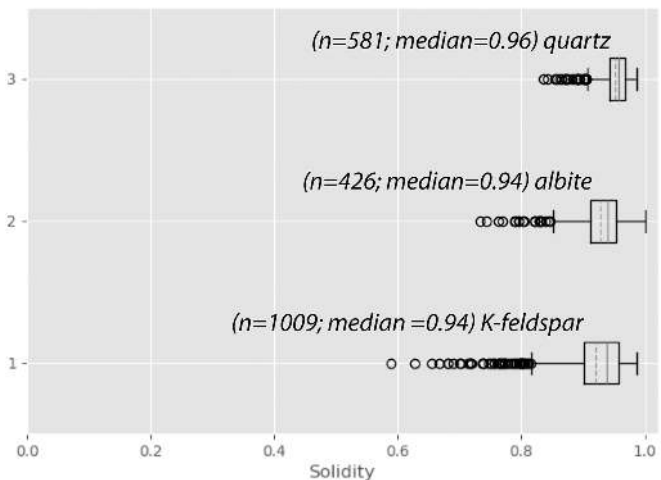
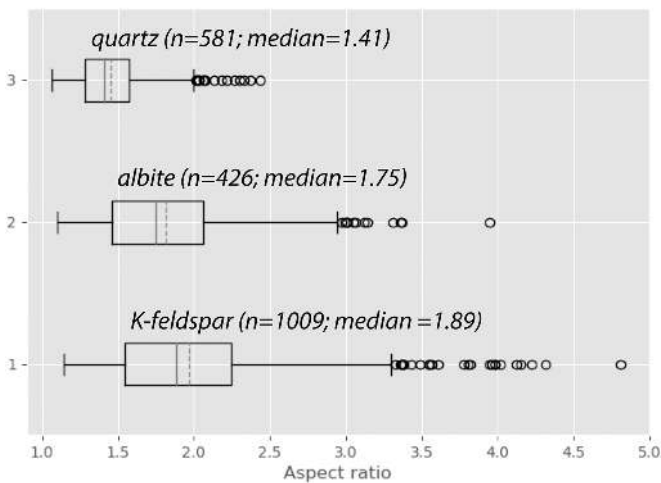
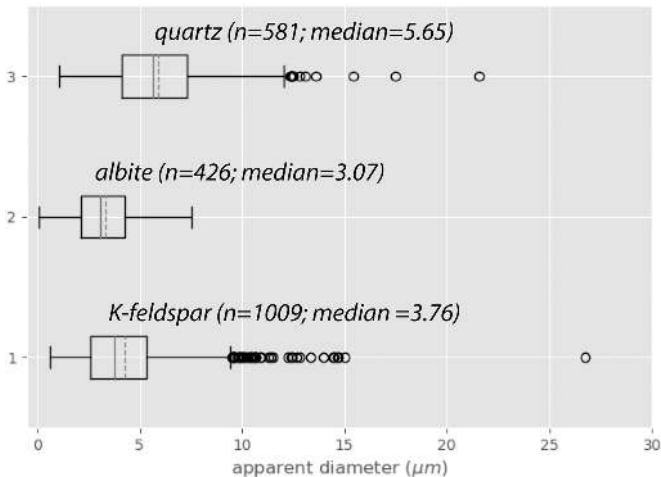


Figure 9

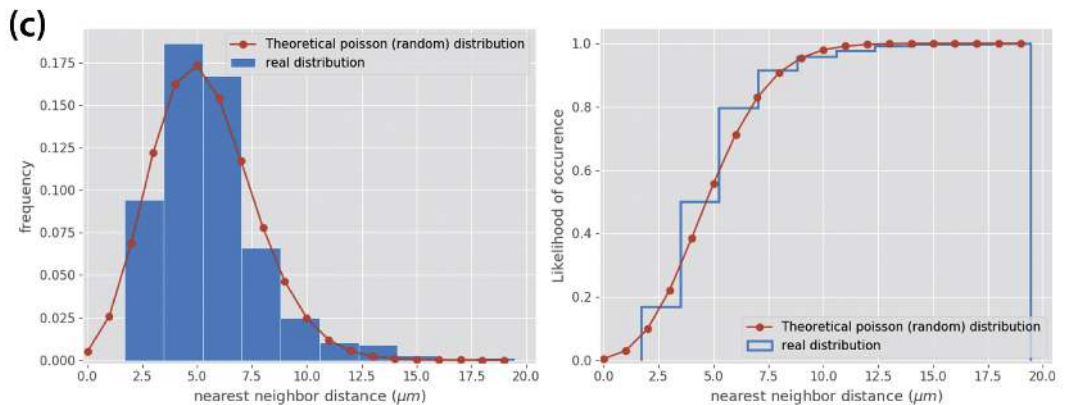
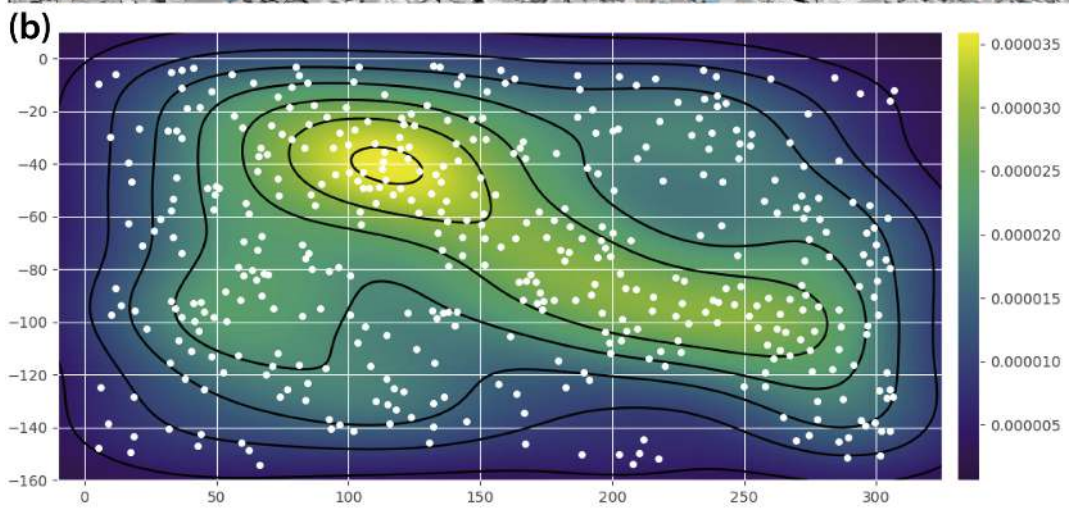
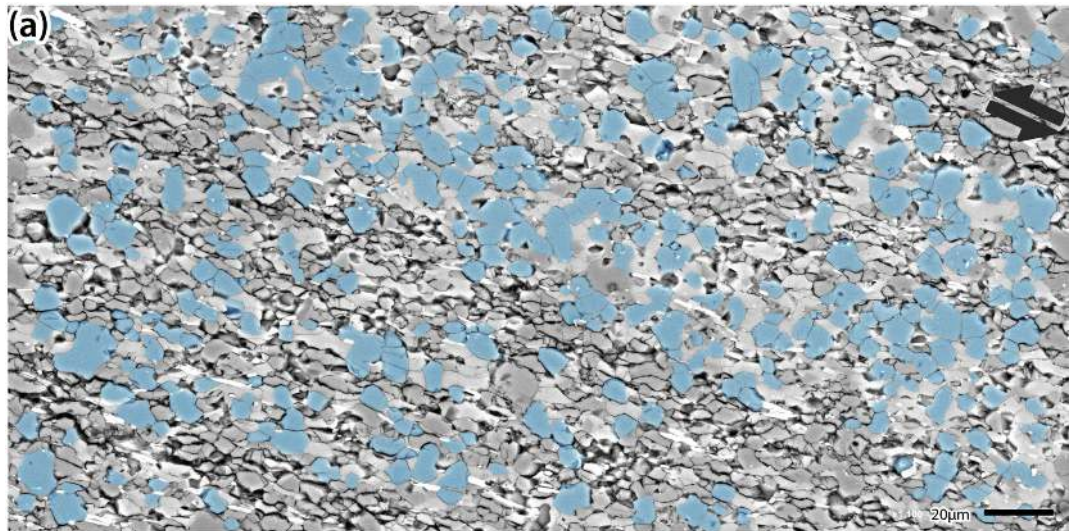


Figure 10

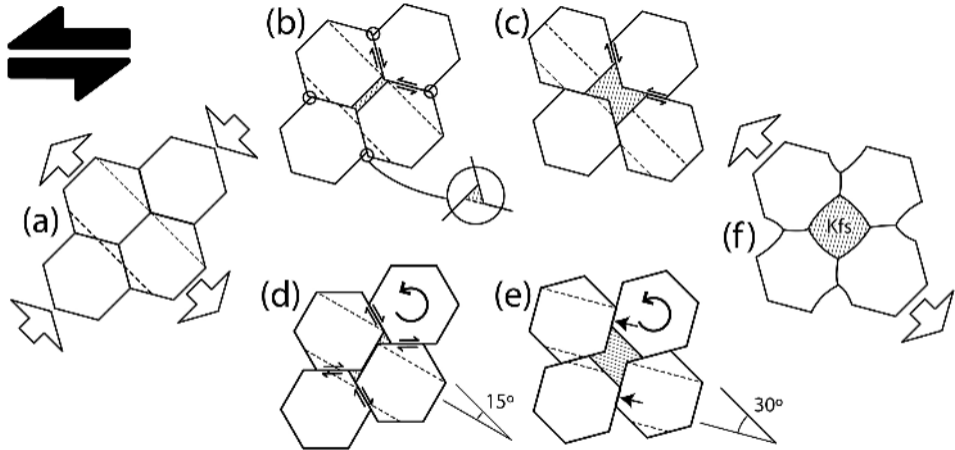


Figure 11

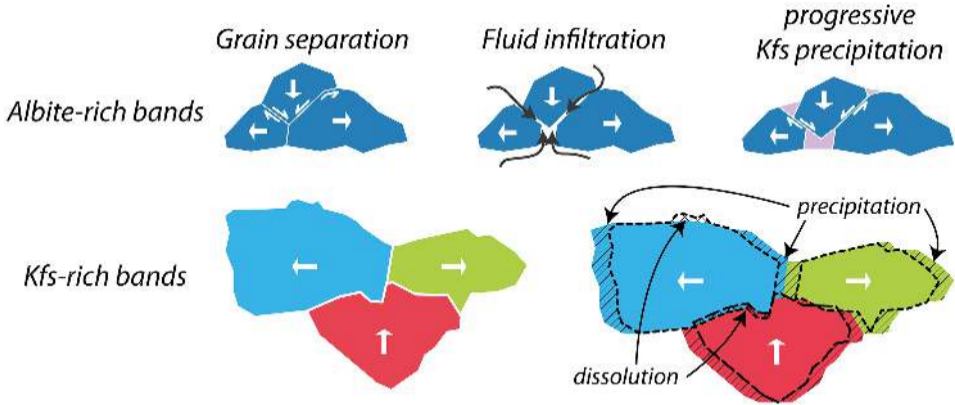


Figure 12

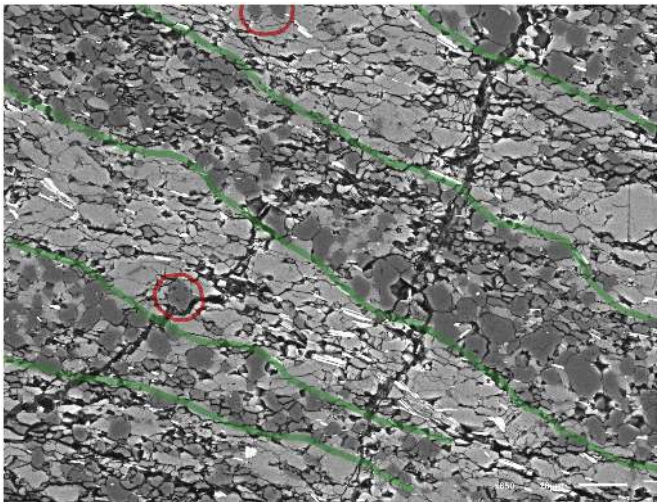


Figure 13

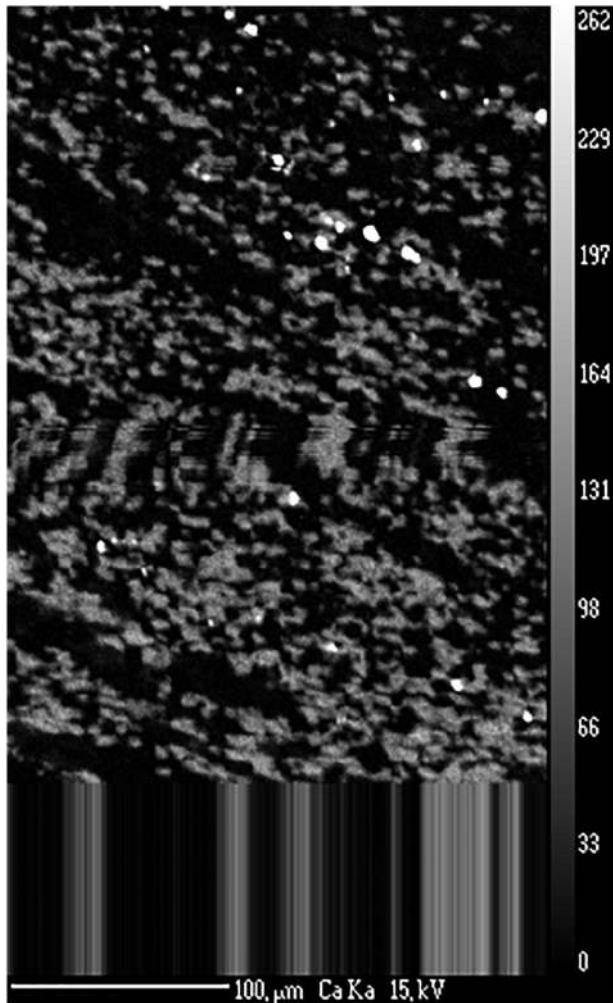


Figure 14

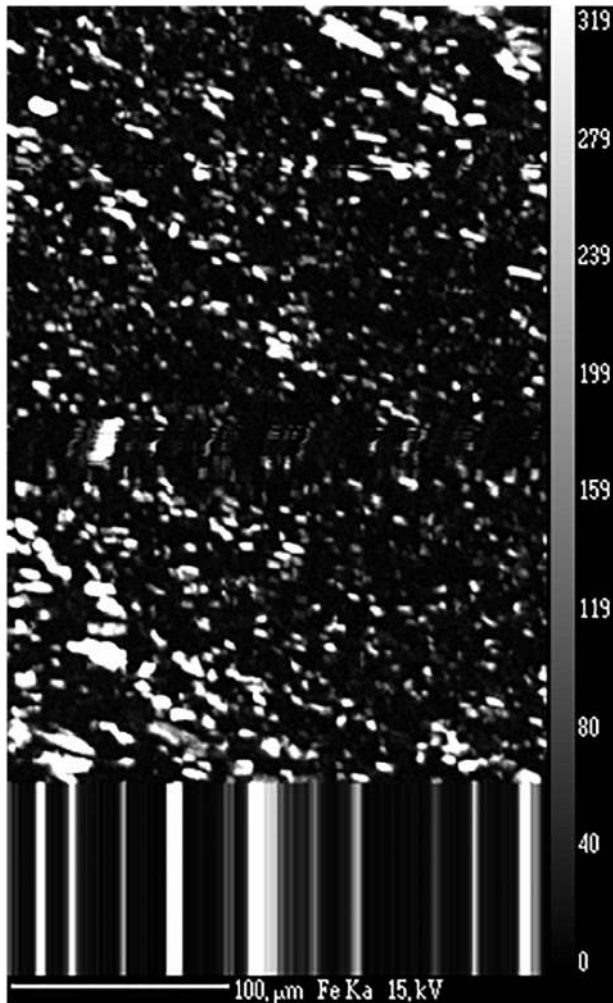


Figure 15

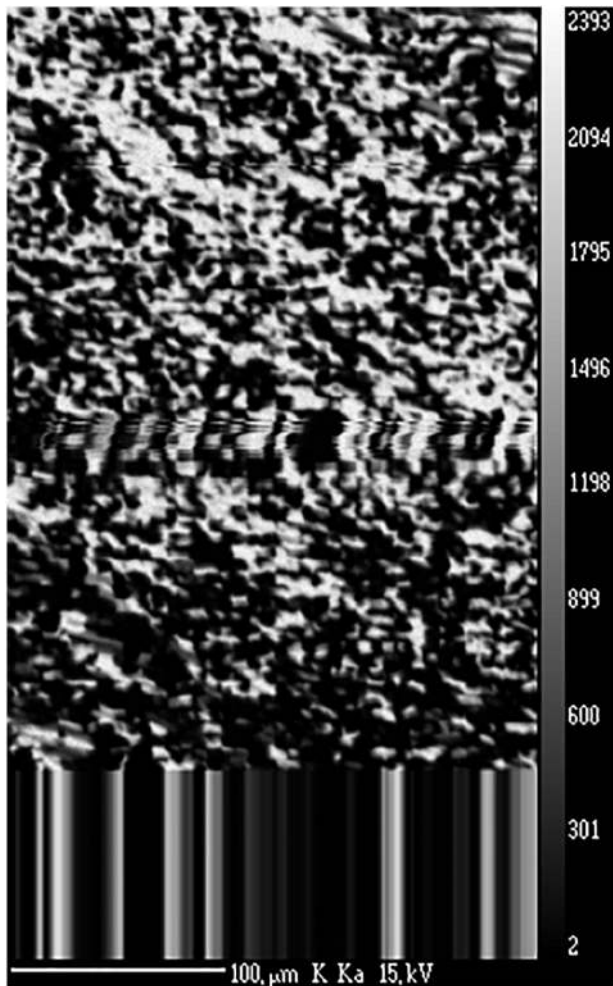


Figure 16

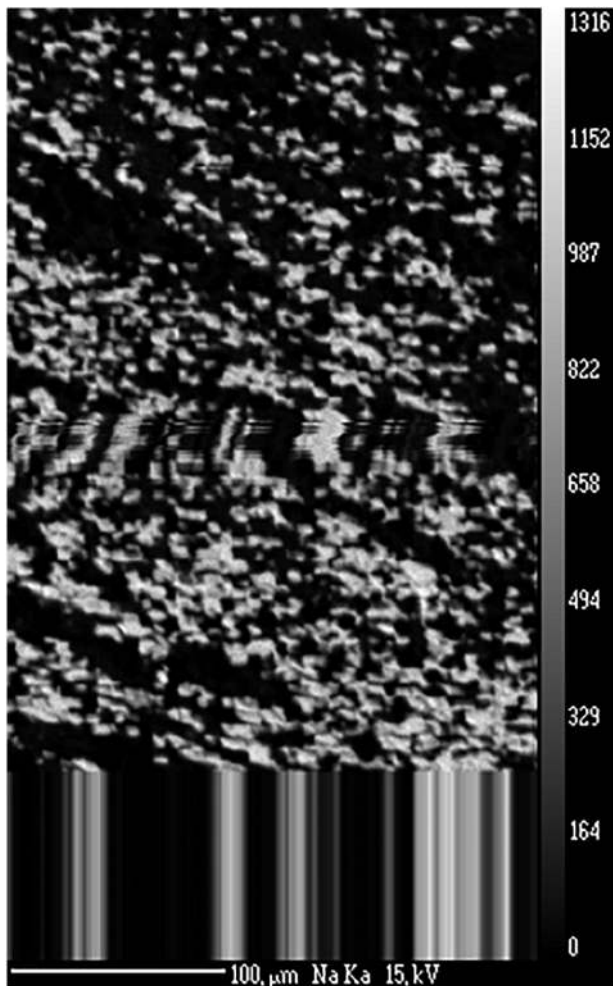


Figure 17

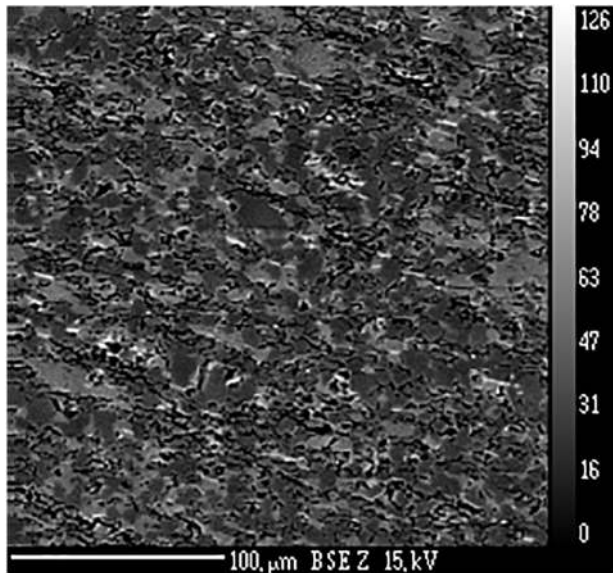


Figure 18

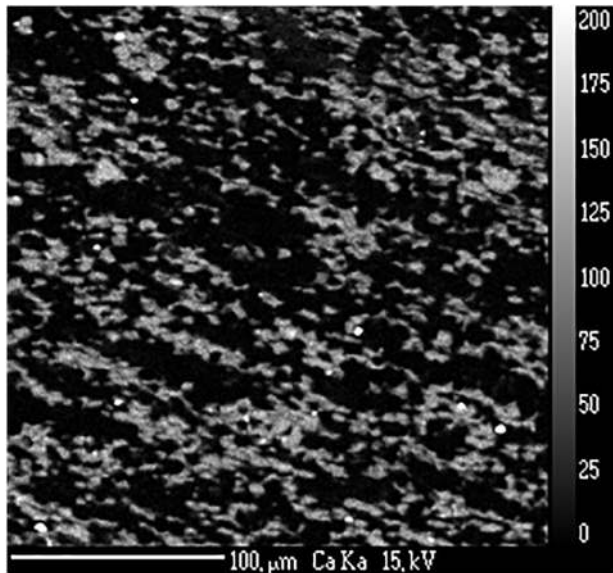


Figure 19

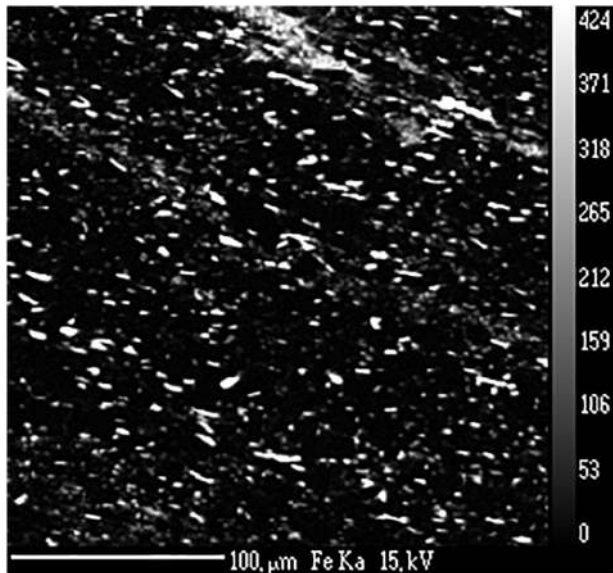


Figure 20

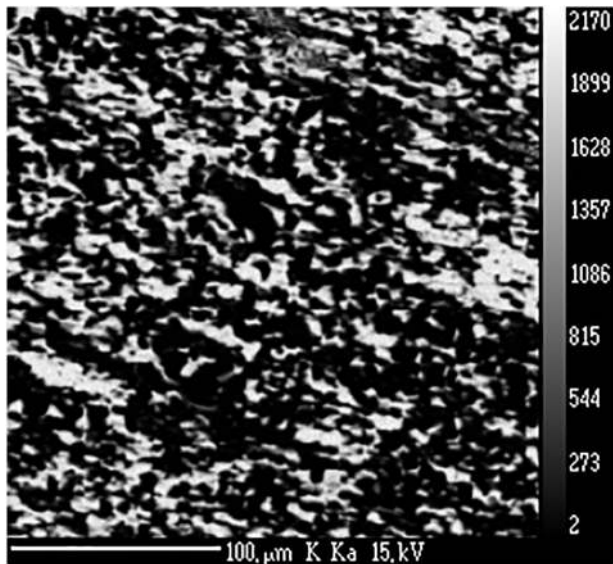


Figure 21